Original Article

Inflow-rotor interaction in Tesla disc turbines: Effects of discrete inflows, finite disc thickness, and radial clearance on the fluid dynamics and performance of the turbine

Sayantan Sengupta ⓘ and Abhijit Guha

Abstract

The article establishes the physics of the complex interaction of discrete multiple inflows with the stationary shroud and the rotating channel of a Tesla disc turbine. Using a large number (150) of separate, fully three-dimensional computational fluid dynamic simulations, we demonstrate the (sometimes dramatic) role of four important input parameters, namely the number of nozzles (N_{nozzle}), rotational speed of the discs (Ω), radial clearance between the rotor and the shroud (Δ_{rc}), and disc thickness (d_t), in the fluid dynamics and performance of a Tesla turbine. An increase in N_{nozzle} or Δ_{rc} assists in the attainment of axisymmetric condition at rotor inlet. Ω influences significantly the distribution of radial velocity including the fundamental shape of its z-profile (parabolic, flat or W-shaped). The paper demonstrates the existence of an optimum Δ_{rc} for which the efficiency of the rotor (η) is maximized. Present computational fluid dynamics simulations for many combinations of N_{nozzle} and Ω establish that the η versus Ω curves, for each fixed value of N_{nozzle}, are of the shape of an inverted bucket. With increasing N_{nozzle}, the operable range of Ω decreases, the buckets become more peaky and the maximum possible η increases substantially (by a factor of 2 in the example calculation shown). The present systematic work thus demonstrates quantitatively, for the first time, that an axisymmetric rotor inflow condition represents the best possible design for the rotor. It is further shown that, as the disc thickness is increased, the efficiency may decrease substantially (even dramatically) and its maxima occur at lower rotational speeds. Chamfering of the disc edge or partial admission decreases the turbine efficiency. Thus, small disc thickness, flat disc edge, full nozzle opening, optimum radial clearance, and inlet condition as close to axisymmetry as is possible are recommended for the design of an efficient Tesla disc turbine.

Keywords

Tesla turbine, co-rotating discs, nonaxisymmetry, computational fluid dynamics, efficiency, power

Date received: 7 July 2017; accepted: 10 January 2018

Introduction

A Tesla disc turbine has two major components – the rotor and the inlet-nozzle assembly. In a previous experimental and theoretical study, Guha and Smiley[1] have described a method for designing the inlet-nozzle assembly such that the loss of total pressure in this component is reduced drastically (as compared to its traditional designs) and the uniformity of the fluid jet that comes out of the nozzle is greatly enhanced. Similarly, by combining the powers of similitude analysis and computational fluid dynamics, Guha and Sengupta[2] have formulated a systematic methodology for designing the most efficient rotor on its own. The present paper bridges the gap

by providing a systematic study on the interaction of the nozzle (or a set of nozzles) with the rotor of the turbine. In particular, the present paper examines the effects of the number and arrangement of discrete nozzles, used in many implementations, on the fluid dynamics taking place in the rotor and, on its

Department of Mechanical Engineering, Indian Institute of Technology Kharagpur, Kharagpur, West Bengal, India

Corresponding author:
Abhijit Guha, Department of Mechanical Engineering, Indian Institute of Technology Kharagpur, Kharagpur 721302, West Bengal, India.
Email: a.guha@mech.iitkgp.ernet.in

performance and efficiency. The existence of discrete nozzles makes the inflow boundary condition nonaxisymmetric (almost all previous journal papers giving theoretical analysis of Tesla turbine assume axisymmetry).

There are two other aspects, which necessarily arise in any practical implementation of a Tesla disc turbine but have been ignored in the theoretical studies conducted over the past 70 years or so. These are the finite thickness of the discs and (a small but finite) radial clearance between the rotor and the shroud. The synthesis of a third aspect also rests on an innovative design reflection on the finite thickness of the discs. One may hypothesize that a jet-like inflow hitting directly the solid edges of the discs would be wasteful and thus an improved design would be to use partial admission of the fluid through the shroud. Instead of being continuous in the direction parallel to the rotor axis, each nozzle would produce $n_d - 1$ number of discrete jets (where n_d is the number of discs), punctuated by gaps whose thickness matches with the thickness of each disc, hoping that in this way the inflow can effectively be directed only through the inter-disc spacings. A second hypothesis involves contouring the edges of the discs (e.g. using a chamfered (tapered) tip) so that the generation of work-absorbing shear stress on the disc edges can be reduced, thereby improving the performance. This paper provides the first systematic study of the effects of finite disc thickness, shape of the disc edge, radial clearance, and partial admission on the fluid dynamics and performance (including efficiency) of a Tesla disc turbine. It is found that sometimes apparently small features can have major impact on both dynamics and performance and, sometimes, the outcome may even be counter-intuitive. Because of the comprehensiveness of the study, design optimization has also been possible.

The Tesla disc turbine was patented[3] by the renowned scientist Nikola Tesla in 1913. The rotor of this turbine comprises a stack of flat, parallel, coaxial discs which are closely-spaced (the gap being $\sim 100\,\mu m$) and attached to a central shaft. Figure 1 shows a schematic of the rotor surrounded by discrete inlet-nozzles embedded in a stationary shroud. Any nozzle of the inlet nozzle assembly occupies only a small portion ($\sim 2^\circ - 6^\circ$) of the whole periphery (i.e. 360°) of the rotor. The exit port of a nozzle is attached to a stationary shroud which encloses the rotor. The shroud-wall, accommodating the exit ports of nozzles, is discontinuous. A small radial clearance is maintained between the stationary shroud and the rotor. Working fluid is injected nearly tangentially into the small passage between the stationary shroud and the rotor. Due to a nonzero (inward) radial velocity component, the fluid in this narrow passage enters into the
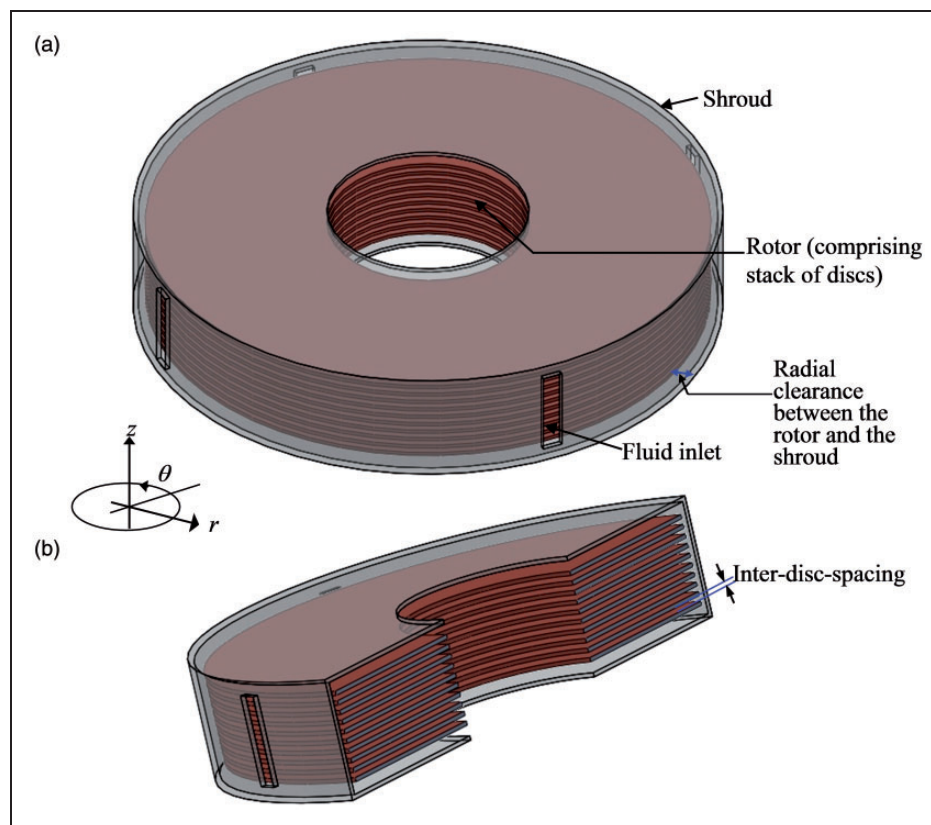

Figure 1. Schematic diagram of the physical configuration comprising shrouded co-rotating discs with superposed inflow through discrete multiple inlets: (a) full view; (b) sectional view.

inter-disc-spacings and approaches towards the exhaust port located at the center of each disc. Due to a transfer of angular momentum from the fluid to the (flat and circumferential) disc-surfaces, a torque is imparted on the rotor. This toque becomes useful in power production when the rotor rotates. However, the torque, which is applied on the stationary shroud by the fluid, is wasted.

After the success of Whittle and von Ohain, the gas turbine became the centerpoint of research and development and the understanding of its performance and optimization has reached quite a mature stage.[4–6] The understanding of the performance of Tesla turbines is not nearly as thorough. The advances in Tesla disc turbine up to 1991 can be found in Rice.[7] A good survey containing present researches on Tesla disc turbine and related aspects of rotating flow is found in Guha and Sengupta.[8] The Tesla disc turbine has several advantages. Other than its manufacturing simplicity and low cost, the Tesla disc turbine is capable of generating power with a variety of working media like Newtonian fluids, non-Newtonian fluids, mixed fluids and two-phase mixtures (a body of relevant physics of two-phase flow is available in various studies[9–13]). In case of nonconventional fuels like biomass, which produce solid particles or, in case of low-quality wet steam operating condition producing vapor–droplet mixture (which may be encountered while utilizing geothermal energy or low-grade waste heat energy), conventional turbines may suffer from blade erosion. In such operating conditions, a bladeless Tesla turbine may be suitable due to its self-cleaning nature. Tesla turbines may be used as a component of a Rankine cycle for small-scale power production.[14,15]

Detailed experimental studies are available in Guha and Smiley,[1] Hoya and Guha,[16] and Lemma et al.[17] An effective technique for measuring the net power output and overall loss called the angular acceleration method is developed by Hoya and Guha,[16] which is particularly useful for high angular speed and low-torque operating conditions. A systematic attempt of experimentally determining (hence optimizing) turbine performance as functions of various parameters such as disc spacing, number of discs, inlet flow angle, nozzle area, rotational speed, etc. is described in McGarey and Monson.[18]

Previous theoretical studies[8,19–24] considered that the flow field within the narrow inter-disc spacing of a Tesla disc turbine is axisymmetric which may be realized either by increasing the number of inlet nozzles or by using a plenum chamber arrangement at the inlet of the rotor. The assumption, axisymmetry, makes it possible to achieve simplified theoretical models or less-expensive computational solutions. However, in many experimental studies, including the recent studies conducted by Hoya and Guha,[16] Guha and Smiley,[1] Zhao et al.,[25] and others, either single or a few (e.g. up to 4) inlet nozzles are used. Such arrangements always produce complex,

nonaxisymmetric, three-dimensional flow pattern within the rotating micro-channels of a Tesla turbine. An initial attempt was made in Lampart and Jedrzejewski[26] to calculate such flow fields for a finite number of nozzles using computational fluid dynamics (CFD) simulations. However, Lampart and Jedrzejewski[26] did not investigate the effects of radial clearance space (between the shroud and the rotor), partial admission, finite disc thickness and shape of the disc edge.

In some other context, the flow in shrouded co-rotating discs has been discussed by a number of previous researchers and, many flow features are explained in Abrahamson et al.,[27] Schuler et al.,[28] Huang and Hsieh,[29] Wu,[30] and Soong et al.[31] Abrahamson et al.,[27] in their experimental investigation with shrouded co-rotating discs, observed three distinct regions of flow, namely an inner region near the hub acting as a solid-body, an outer region dominated by large counter-rotating vortices, and a boundary layer region near the shroud. Huang and Hsieh[29] employed particle image velocimetry (PIV) and observed five characteristic regions (solid-body rotation region, hub-influenced region, buffer region, vortex region, and shroud-influenced region). Wu[30] also employed PIV and quantitatively identified the shroud-influenced region. Hendriks[32] and Shirai et al.[33] showed that the knowledge acquired from the study of flow in shrouded co-rotating discs is useful in understanding the aerodynamics of hard disc drives. The present flow configuration is different from the configurations considered in various studies.[27–33] In these references,[27–33] the fluid is driven by the rotational motion of the discs, whereas in the present case, the fluid drives the disc-surfaces. Additionally, in the present case, there is a superposed inward flow by discrete multiple nozzles set at the periphery of the shrouded discs.

According to Czarny et al.,[34] while the geometry may be strictly axisymmetric, it is possible to have nonaxisymmetric patterns for turbulent (and unstable) flow adjacent to rotating discs. Several studies are available in the literature dealing with nonaxisymmetric flow in an axisymmetric geometric-configuration formed by parallel, coaxial discs. Czarny et al.[34] showed nonaxisymmetric flow patterns in a rotor–stator disc cavity; Nore et al.[35] showed nonaxisymmetric flow patterns between exactly counter-rotating discs; and Hewitt and Al-Azhari[36] found nonaxisymmetric flow between two independently rotating infinite, parallel discs. We, however, consider laminar flow. Nonaxisymmetry, in the present study, arises due to the presence of a stationary shroud and discrete inlets in the flow configuration.

In our previous theoretical studies and computational investigations,[2,19,20,23,24,37] we dealt with Tesla turbines under axisymmetric inflow condition. Theoretical work of other researchers also assumed axisymmetric inflow condition. A collection of our

previously published CFD and analytical results for axisymmetric inflow condition, and their mutual comparison and validation with available experimental data are displayed in Figure 2. In the present paper, the CFD method is generalized to deal with nonaxisymmetric physical configurations with finite discrete inflows. This enables us to formulate generalized flow physics and design principles that go far beyond what can be established from a study with axisymmetric inflow. The present paper shows how the results of nonaxisymmetric simulations approach those of axisymmetric analysis as the number of discrete inflows is progressively increased, and establishes an important new conclusion that in order to achieve the best possible efficiency of the Tesla disc turbine it is necessary to achieve axisymmetric inflow to the rotor, thus

retaining the usefulness of the physical understanding developed in our previous axisymmetric studies.[2,19,20,23,24,37]

The complex interaction of the discrete multiple inflows within the small radial clearance space between the shroud and the rotor, the interesting spatial evolution during the subsequent flow through the rotor–rotor cavity, the attainment of a nearly axisymmetric distribution towards the outlet, and the critical role of axisymmetry on the performance of a Tesla turbine have been investigated in this paper. We examine the effects of the number of nozzles N_{nozzle}, the rotational speed of the discs (Ω), the radial clearance between the rotor and the shroud (Δ_{rc}), the finite disc thickness (d_t), the shape of the disc edge, and the partial admission on the fluid dynamics and
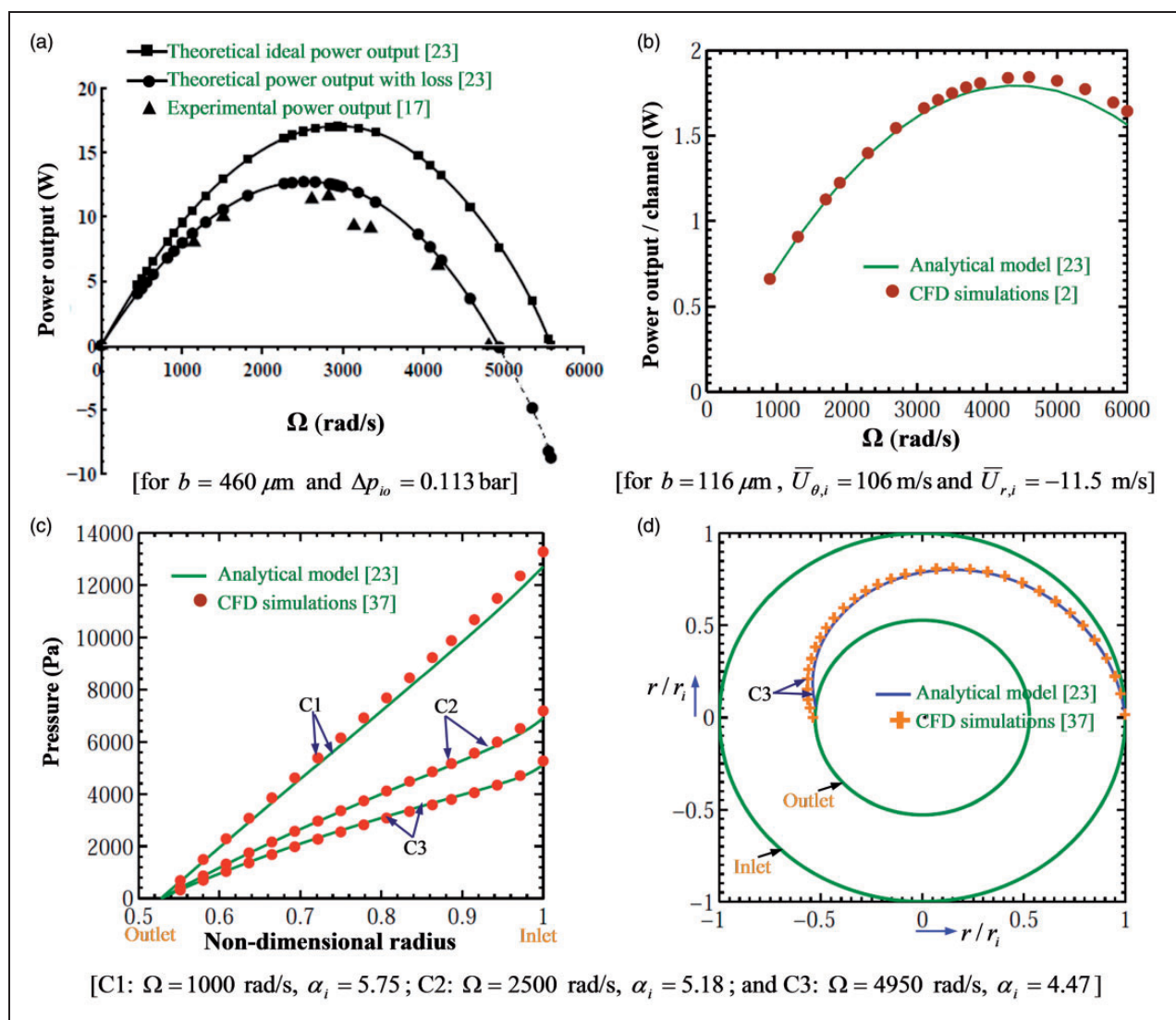

Figure 2. Results obtained for a Tesla turbine operated under an axisymmetric inflow condition, and their comparison and validation: (a) power output predicted by the analytical model[23] versus the power output found in the experiment[17] with a 9-disc-rotor; (b) a comparison of power output/channel: CFD simulations[2] versus the analytical model,[23] (c) a comparison of pressure on the middle (z-) plane of an inter-disc-spacing: CFD simulations[37] versus the analytical model,[23] (d) a comparison of pathlines on the middle (z-) plane of an inter-disc-spacing: CFD simulations[37] versus the analytical model.[23] (All results correspond to $r_i = 0.025$ m, $r_o = 0.0132$ m, $d_t/b = 0$, $\Delta_{rc} = 0$ and air as working fluid.)

performance of Tesla turbines. In order to capture the physics thoroughly, a large number (150) of separate, fully three-dimensional, CFD simulations are performed on a fine grid, necessary to capture the fluid dynamics at a small scale inside the clearance space. Each CFD simulation is run to a high degree of convergence (maximum root mean square (RMS) residual being 10^{-6}). The CPU time for each simulation varied from about 4 h to about 32 h, run on a cluster (x86-64 architecture and 198 GB RAM) of 16 processors (Intel(R) Xeon(R) CPU E5-4640 with base frequency of 2.40 GHz). Such a comprehensive set of high-precision, fully three-dimensional (nonaxisymmetric) resource-intensive computations has not been attempted in the past.

Method of CFD simulations

A commercially available CFD software CFX 15 is used to solve the Navier–Stokes equations in the computational domain (the details of computational domain are given later in this section). The set of equations[38] are as follows.

Continuity equation

$$\frac{\partial \rho}{\partial t} + \nabla \cdot \left(\rho \vec{U} \right) = 0 \tag{1}$$

Momentum equations

$$\frac{\partial \left(\rho \vec{U} \right)}{\partial t} + \nabla \cdot \left(\rho \vec{U} \otimes \vec{U} \right) = -\nabla p + \nabla \cdot \tau \tag{2}$$

Energy equation

$$\frac{\partial (\rho h_t)}{\partial t} - \frac{\partial p}{\partial t} + \nabla \cdot \left(\rho \vec{U} h_t \right) = \nabla \cdot (\lambda \nabla T) + \nabla \cdot \left(\vec{U} \cdot \tau \right) \tag{3}$$

where $\vec{U}$ is the velocity vector, p is the gage value of static pressure, and T is the temperature. τ is the stress tensor, expressed as follows

$$\tau = \mu \left(\nabla \vec{U} + (\nabla \vec{U})^T - \frac{2}{3} \delta \nabla \cdot \vec{U} \right) \tag{4}$$

In equation (3), $\nabla \cdot (\vec{U} \cdot \tau)$ represents the work due to viscous stresses and is called the viscous work term. h_t is the total enthalpy, related to the static enthalpy, $h(T, p)$ by $h_t = h + \vec{U}^2 / 2$. The effect of gravity is neglected in the analysis.

Air is used as working fluid. The dynamic viscosity μ, thermal conductivity λ, constant pressure specific heat capacity c_p are considered to be constant. The values of μ, λ and c_p used here are adopted for a reference state (at 25°C and 1 atmospheric pressure). The density of air, ρ, is modeled by the equation

of state for an ideal gas. The equation of state for an ideal gas is as follows

$$\rho = p_{abs}/RT \tag{5}$$

where p_{abs} is the absolute pressure (the gage pressure being denoted by p); R is the specific gas constant of air (the ratio of the universal gas constant to the molecular weight of air).

CFX 15 is an element-based finite volume solver. Navier–Stokes equations (equations (1) to (4)) are solved for finite volumes which are generated by discretizing the spatial domain into a mesh of discrete nodes. CFX 15 uses finite element shape functions to calculate the velocity and pressure at integration points from the velocity and pressure at mesh nodes. CFX 15 uses co-located grid and therefore, special techniques proposed by Rhie and Chow[39] are implemented to avoid the formation of a decoupled (checkerboard) pressure field. The detailed procedure and solution methodology are given in the theory guide of ANSYS CFX.[38] Shape functions are used to evaluate spatial derivatives for all the diffusion terms. To evaluate the advection terms at the integration points, the high resolution scheme; whose spatial order may vary between one and two, is utilized. The coupled solver of CFX 15, which solves the equations (for U_x, U_y, U_z, p, etc.) as a single system, is used. At any given time step, a fully implicit discretization of the equations is adopted. Present paper gives the steady-state solutions. The time-step, for steady-state problems, behaves like an "acceleration parameter", to guide the approximate solutions in a physically based manner to a steady-state solution.[38] Double-precision arithmetic is adopted for all numerical calculations given in this paper.

The physical configuration is shown in Figure 1. The rotor consists of a stack of discs (generally 10 to 20 discs). Instead of solving the flow field for the full rotor, we have considered only two consecutive discs of the full rotor assuming the flow characteristics between any two consecutive discs of the rotor are the same. This assumption is not strictly applicable in the region between the end discs and the casing where the flow field is similar to the flow field within a stator–rotor. However, the effect of the end-discs on the overall fluid dynamics and torque generation is not significant when the number of discs is large.

The computational domain, comprising the two successive discs, is shown in Figure 3. The inter-disc-spacing is denoted by b and the disc thickness is denoted by d_t. The maximum and the minimum z-coordinates of the computational domain are defined by the two symmetry planes. Each symmetry plane divides the respective disc-edge axially into two halves. Thus the total axial extent of the domain is $b + d_t$. Each disc has an outer radius r_d and an inner radius r_o (subscript o denotes the location of the rotor outlet). Both the shroud-wall and the discrete inlets
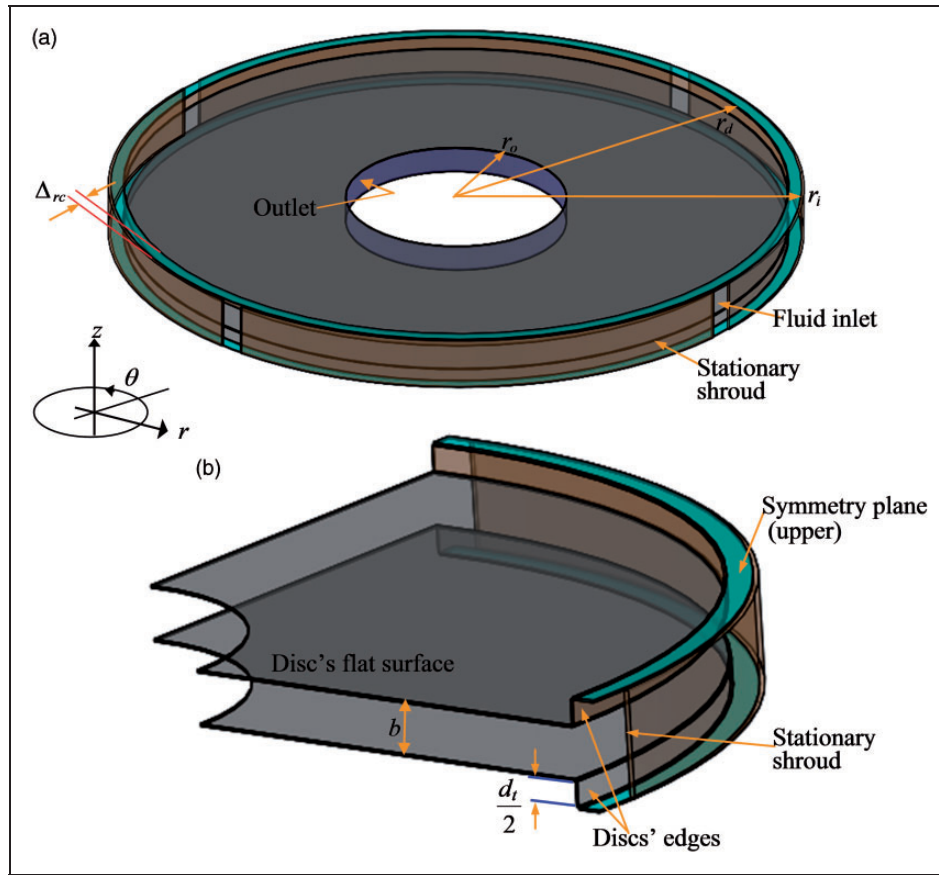
Figure 3. Schematic diagram of the computational domain between two co-rotating discs: (a) full view; (b) sectional view. (The inter-disc-spacing, in relation to the radius, is exaggerated in the sketch for clarity.)

are located at the same circumferential plane which is positioned at radius r_i. A small radial clearance is maintained between the discs and the circumferential plane containing the shroud-wall and the discrete inlets. The radial clearance is denoted by Δ_{rc} ($\Delta_{rc} \equiv r_i - r_d$). In the present CFD simulations, the geometric parameters r_d, r_o, and b are fixed; their values being $r_d = 25$ mm, $r_o = 13.2$ mm, and $b = 300$ μm. For most of the simulations, r_i is set as 25.2 mm. However, while investigating the role of Δ_{rc}, the value of Δ_{rc} is changed by varying the value of r_i. The objective is to investigate the effect of varying Δ_{rc} for a fixed size of the rotor. One set of simulations is run for $d_t = 0$, and the other set is run for finite d_t. The azimuthal extent covered by each inlet is 4°. The locations of the inlet nozzles are such that they divide the shroud wall into a finite number of identical parts. For example, in a 4-inlet configuration ($N_{nozzle} = 4$), the inlet nozzles divide the shroud wall into four identical parts (see Figure 3).

The following boundary conditions are adopted to obtain CFD solutions presented in this paper. (i) At the inlets, mass flow rate ($\dot{m}_i$), flow angle (α_i), and total temperature ($T_{t,i}$) are specified. The study is conducted for a constant value of mass flow rate through the outlet ($\dot{m}_o = 3 \times 10^{-5}$ kg/s per rotating channel); each inlet is assumed to inject identical amount of mass flow rate, therefore $\dot{m}_i = \dot{m}_o / N_{nozzle}$. In most of

the simulations, the full axial extent of the inlet opening is available for the fluid's admission; partial admission is, however, used for one set of computations. Unless otherwise specified, we consider $T_{t,i} = 313$ K, and, $\alpha_i = 6°$ with the tangential direction. Due to nonzero α_i, the velocity vector at the inlet has tangential and radial components, denoted respectively by U_θ and U_r. (ii) At the outlet, the gage value of static pressure is zero. (iii) At the stationary wall of the shroud, no-slip condition is specified. (iv) No-slip condition, with a rotational speed Ω, is set on the disc flat surfaces and on the disc edges. (v) The upper and lower circular strips extended from r_d to r_i (see Figure 3) are modeled with "symmetry" boundary condition.

We present the CFD solutions for steady, laminar, subsonic flow. To maintain subsonic flow, Mach number is kept less than 1 (the maximum being 0.66). To maintain laminar flow, the dynamic similarity number Ds ($Ds \equiv |U_{r,i}| b^2 / \nu\, r_i$) is kept below 10,[8,19] where $U_{r,i}$ is the radial velocity at the inlet and ν is the kinematic viscosity of the working fluid. A maximum RMS residual[38] of 10^{-6} is used as the convergence criterion for the present study.

Grid-independence test has been carried out separately for each flow configuration (i.e. for each value of N_{nozzle}). Table 1 shows a few pertinent details for $N_{nozzle} = 4$, overall features of the grids for other

Table 1. Grid independence test (for $N_{nozzle} = 4$, $\dot{m}_o = 30$ mg/s, $\Omega = 2000$ rad/s, $\alpha_i = 6°$, $T_{t,i} = 313$ K, $\Delta_{rc} = 0.2$ mm, $d_t/b = 0$).

Grid distribution	Number of grids in r, θ, and z directions	Total number of cells	Power output obtained from a single rotating channel (W)	Area-averaged p (gage value) at one of the four inlets (Pa)
Coarse	$(130 \times 220 \times 40)$	1,144,000	0.0892	1345
Standard	$(208 \times 340 \times 60)$	4,243,200	0.0864	1317
Fine	$(270 \times 400 \times 75)$	8,100,000	0.0872	1312

Table 2. Details of fine grid distributions for various flow configurations.

Flow configuration	Details of fine grid distribution	Number of grids in r, θ, and z directions
2-nozzle	10,432,800	$(322 \times 360 \times 90)$
4-nozzle	8,100,000	$(270 \times 400 \times 75)$
8-nozzle with $d_t/b = 0$	6,489,600	$(208 \times 520 \times 60)$
8-nozzle with $d_t/b = 1, 2, 3$	8,153,600	$(208 \times 520 \times 60) +$ $(40 \times 520 \times 80)$
16 nozzle	5,734,400	$(200 \times 512 \times 56)$

values of N_{nozzle} being summarized in Table 2. We have used mapped, hexahedral computational cells for the results presented in this paper. The grids are distributed differently in the r, θ, and z directions in accordance with the difference in the flow physics in the three directions. The grid distribution in the z-direction is nonuniform with very small grid size close to the flat surfaces of the two discs (to capture the velocity gradient on the surface accurately) and with progressively larger grid size towards the middle of the inter-disc-spacing and towards the symmetry planes. Between two consecutive inlets, the grids in the θ-direction are nonuniformly distributed. Very small grid is used at the junction of any inlet and its adjacent shroud-wall. The grid-size, starting from the end of a particular inlet opening, increases progressively along the shroud wall, attains a maximum value in the midway, and then decreases progressively in the vicinity of another inlet opening. Uniform grid distribution is taken within the small azimuthal extent (i.e. 4°) of any inlet. In the r-direction, the grids are divided into two zones—nonuniform and uniform. In order to capture the boundary layers attached to the stationary shroud and the rotating discs, very small grid-size is used near the inlet, and the grid distribution is nonuniform near the inlet. The rest of the radial extent up to the outlet is meshed uniformly. Table 1 indicates that after attaining the standard grid distribution, any further grid refinement results into insignificant changes

of the output parameters. We, however, present the results obtained for the fine grid distribution. Some relevant details of the fine grid distributions used in various flow configurations are given in Table 2.

Synthesis of fluid dynamic principles from the computed results

In a systematic study of a complex system in which several parameters need to be varied, certain overall characteristics of the system should be kept fixed so that a meaningful generalization from a large set of output data is possible. In the present study, therefore, the same values of overall mass flow rate ($\dot{m}_o$) per rotating channel, total temperature at inlet ($T_{t,i}$) and flow angle at inlet (α_i) are preserved for all computations. To bring order in comprehension, the disc is assumed to be of negligible thickness ($d_t \rightarrow 0$) for the first three sub-sections below. The effects of varying the number of nozzles (N_{nozzle}), rotational speed of the discs (Ω) and radial clearance between the rotor and the shroud (Δ_{rc}) on the fluid dynamics within the turbine are examined in these three sub-sections. The effects of varying the thickness ratio (d_t/b) on the fluid dynamics are examined in the fourth sub-section. An important point to comprehend the various two-dimensional contour plots given in this section is to constantly reflect on the influence of the velocity component which is perpendicular to the plane in which contours are plotted. The basic three-dimensionality of the flow field gives rise to this complexity. As an example, while interpreting the distribution of radial velocity on a selected $r - z$ plane, transport of mass and momentum by the tangential velocity should be kept in mind.

Role of the number of nozzles (N_{nozzle})

This section investigates the effect of varying N_{nozzle} on the flow field while all other input parameters, namely $\dot{m}_o$, d_t/b, Ω, α_i, $T_{t,i}$, and Δ_{rc}, are kept fixed. Figure 4 displays the contours of radial velocity (U_r), tangential velocity (U_θ), and static pressure (p), for 2-inlet ($N_{nozzle} = 2$), 4-inlet ($N_{nozzle} = 4$), and 8-inlet ($N_{nozzle} = 8$) configurations. The contours are shown on the mid $r - \theta$ plane of the inter-disc-spacing.
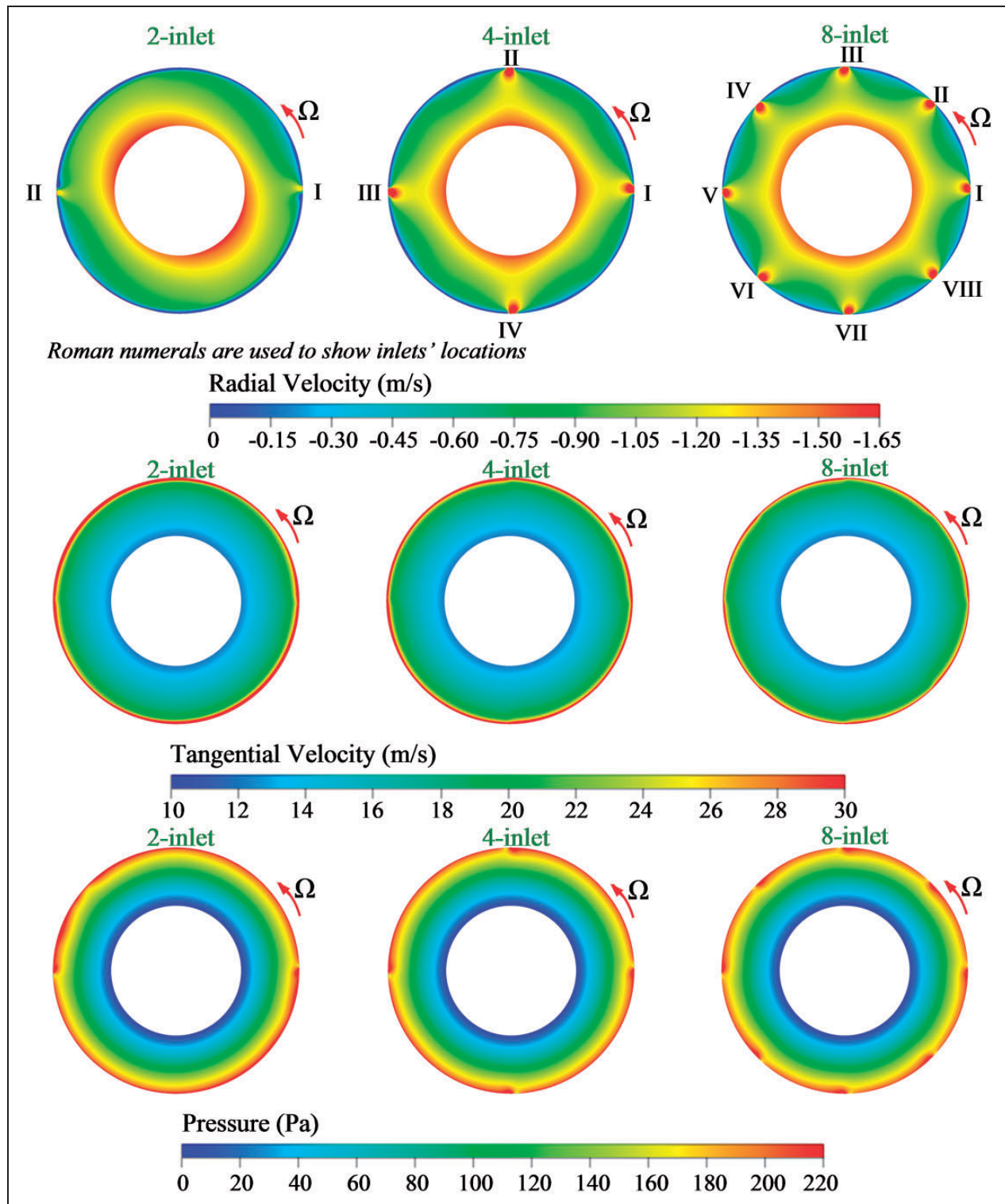
Figure 4. Distributions of tangential and radial velocities and static pressure on the middle-plane of the inter-disc-spacing for three different flow configurations, namely 2-inlet, 4-inlet, and 8-inlet configurations, excluding the solution in the radial clearance space. (For $\dot{m}_o = 30$ mg/s, $d_t/b = 0$, $\Omega_o = 800$ rad/s, $\alpha_i = 6°$, $T_{t,i} = 313$ K, $\Delta_{rc} = 0.2$ mm. The same scales are used for a given flow variable to understand how the flow asymmetry depends on the number of discrete inlet-nozzles; the minimum or maximum of scales shown here does not represent the minimum or maximum of a flow variable in any inlet configuration. As an example, the value of $U_{r,i}$ for 2-inlet is -25 m/s, if we include this value in the contour plots, then the fine details of flow asymmetry shown in this figure cannot be revealed.)

If one moves along a radial line, it is found that U_r (for any nozzle-configuration) at first decreases from its large value at the inlet openings, finally increasing again near the rotor exit. This flow feature is consistent with the equation of continuity. Each inlet occupies only a small azimuthal extent (i.e. 4°). Therefore, in any particular configuration, the sum of the azimuthal extents covered by all the inlets is much less than 360°. For example, for a 4-inlet configuration, this sum is only 16°. In other words, the circular boundary at $r = r_i$ is mostly occupied by the solid shroud-wall. As the fluid moves slightly inward from $r = r_i$, the full 360° extent is available for the fluid flow, due to the absence of the shroud wall. This is why the magnitude of radial velocity has to decrease to satisfy the equation of continuity. The decrease of $|U_r|$ is therefore attributed to an effort of relaxing the azimuthal nonuniformity imposed at $r = r_i$. We now explain why $|U_r|$ increases towards the exit. For $r < r_i$, the available flow area, proportional to r, decreases towards the outlet. The effect of decreasing flow area counteracts the effect of azimuthal spreading near the inlet. This is why, below a certain radius, $|U_r|$ increases for any further decrease in radius. When other input parameters are fixed, nonaxisymmetry decays faster with increasing N_{nozzle}. This feature is demonstrated while comparing the U_r-distribution for an 8-inlet configuration with the U_r-distribution for a 2-inlet configuration (Figure 4).

Figure 4 shows that the near-axisymmetry in the contours of U_θ and p is obtained at a larger radial location, as compared to that in the contours of U_r. This characteristic can be explained in the following way. Consider a relative frame of reference, in which an observer is rotating at the same angular speed as the discs' rotational speed (Ω). The relative tangential velocity is denoted by V_θ; and, $U_\theta = V_\theta + \Omega r$. Out of the two components of U_θ, Ωr is independent of θ. The nonaxisymmetry displayed in the contour plot of U_θ is solely due to the nonaxisymmetric distribution of V_θ. For the adopted geometry and input parameters, V_θ decreases substantially near the inlet, and Ωr becomes the dominant part of U_θ. Although the nonaxisymmetry in V_θ persists much longer along the flow path, axisymmetry in U_θ is approached much earlier (i.e. at a larger radial location) due to the contribution of Ωr.

An interesting flow feature can be most clearly observed in the U_r-contour for the 2-inlet configuration. It is found that the mass flow rate at the rotor exit is not axisymmetric; the most interesting feature of this circumferential variation is that the locations of the greatest mass flow rate at exit do not fall on the radial lines extended from the inlets, but are situated somewhere in between the radial positions of two consecutive inlets. Transport of mass by the significant amount of tangential motion is responsible for this phenomenon.

Role of the rotational speed of the discs (Ω)

This section investigates the effect of varying Ω on the flow field while all other input parameters, namely $\dot{m}_o$, d_t/b, α_i, $T_{t,i}$, Δ_{rc}, and N_{nozzle}, are kept fixed. Figure 5 shows the contours of U_r on the middle-plane of the inter-disc-spacing for an 8-inlet flow-configuration ($N_{nozzle} = 8$). Figure 5(a), (b), and (c) displays the contours of U_r for $\Omega = 1000$ rad/s, $\Omega = 1500$ rad/s, and $\Omega = 2000$ rad/s, respectively.

At first, we focus our attention to the region near $r = r_i$, where U_r is nonaxisymmetric because of the presence of discrete inlets. The magnitude of U_r is large adjacent to each of the inlets; and, the magnitude of U_r is small between two consecutive inlets. For $\Omega = 2000$ rad/s, a portion of the large-$|U_r|$-region enters into the small-$|U_r|$-region. Due to such entrainment, the large-$|U_r|$-region looks like a blob with a tail (see Figure 5(c)). Such an interaction between small-$|U_r|$ and large-$|U_r|$-regions does not occur for small values of Ω. Consequently, the tail-like-feature does not appear, e.g. see Figure 5(a) corresponding to $\Omega = 1000$ rad/s. It has already been mentioned that at a short radial distance from $r = r_i$, $|U_r|$ decreases because of the azimuthal spreading, and U_θ also decreases and becomes of the order of Ωr. The value of Ω determines the difference between the magnitudes of U_θ and $|U_r|$ near $r = r_i$. When Ω is large, U_θ is much greater than U_r near $r = r_i$. At large values of Ω, due to the presence of a large tangential momentum, a chunk of fluid adjacent to the inlet region shifts tangentially in the direction of disc-rotation, keeping its radial momentum (which drives the fluid radially inward) intact. Such tangential shift results into the tail-like feature.

We now focus our attention to the region near $r = r_o$. Near $r = r_o$, the distribution of U_r is more or less axisymmetric in nature; and, the value of U_r on the middle plane of the inter-disc-spacing decreases with an increase in Ω. To investigate the reason of the decrease of U_r with increasing Ω, z-variations of U_r are calculated at various Ω. Figure 5(d) shows the z-profiles obtained at $r = 15$ mm and $\theta = 0°$ for the three values of Ω. When $\Omega = 1000$ rad/s, the z-variation is parabolic in nature. In the parabolic distribution, the maximum value occurs at $z/b = 1/2$. When $\Omega = 1500$ rad/s, the z-profile is no longer parabolic. A flat trend is attained near $z/b = 1/2$. With a further increase in Ω, a W-shaped profile is obtained, e.g. see the profile corresponding to $\Omega = 2000$ rad/s. In such W-shaped profiles, two maxima exist while there is a minima at the centerline. The transition from the parabolic to flat to the W-shaped profiles explains why, with increasing Ω, the magnitude of U_r at the centreline decreases near the outlet.

The formation of the W-shaped profiles can be explained as follows. For the representative 8-inlet configuration, axisymmetry is nearly attained near
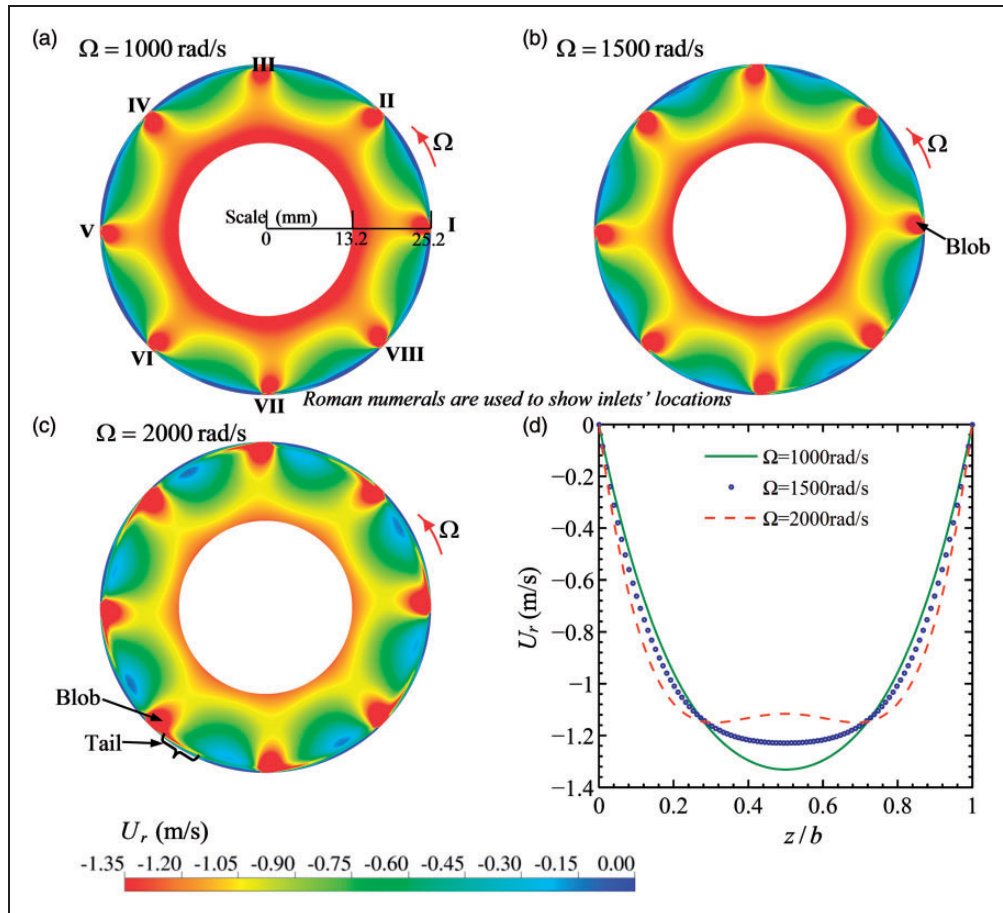
Figure 5. Effect of increasing the rotational speed of the discs (Ω) on the radial velocity distribution: (a) contours for $\Omega = 1000$ rad/s; (b) contours for $\Omega = 1500$ rad/s; (c) contours for $\Omega = 2000$ rad/s; (d) z-variations of U_r at $r = 15$ mm and $\theta = 0°$ obtained for the three representative values of Ω. (For $N_{nozzle} = 8$, $d_t/b = 0$, $\dot{m}_o = 30$ mg/s, $\alpha_i = 6°$, $T_{t,i} = 313$ K, $\Delta_{rc} = 0.2$ mm. All contours are presented on the middle-plane of the inter-disc-spacing.)

the outlet of the rotor and the Mach number in the flow field remains below 0.3. We, therefore, consider the continuity equation for steady, laminar, axisymmetric and incompressible flow.

$$\frac{1}{r}\frac{\partial (rU_r)}{\partial r} + \frac{\partial U_z}{\partial z} = 0 \qquad (6)$$

An integral form of equation (6) is

$$-U_r = \frac{\int \left(\frac{\partial U_z}{\partial z}\right)r\,\delta r}{r} + \frac{c(z)}{r} \qquad (7)$$

The contributions of the viscous effect and total inertia (comprising inertia, Coriolis, and centrifugal terms) in the radial momentum equation would change with a change in Ω.[8] In the subsequent discussion, the total inertia is called inertia for simplicity. When Ω is small, the viscous effect dominates over the inertial effect and the pressure gradient term in the radial momentum equation is principally balanced by the viscous term. The $U_r - z$ profile is then found to be parabolic. In Sengupta and Guha,[23,37] it was shown that when the parabolic profile is a good approximation, the term $(\partial U_z/\partial z)$ can be neglected.

With an increase in Ω, as the inertial effect increases, the first term in the R.H.S. of equation (7) is no longer negligible. At the middle-plane of the inter-disc-spacing, where the viscous effect is expected to be the smallest, this term perturbs the profile considerably. On the other hand, near the disc-surfaces, this term perturbs the profile to a smaller extent. Thus a W-shaped profile is obtained for a large value of Ω.

Role of the radial clearance (Δ_{rc})

CFD simulations are performed for both $\Delta_{rc} = 0$ and $\Delta_{rc} \neq 0$. Representative results are shown in this section for a 2-inlet configuration ($N_{nozzle} = 2$) on the middle-plane of the computational domain. Figure 6 shows the effect of radial clearance on the contours of absolute tangential velocity near the inlet. Figure 6(a) corresponds to $\Delta_{rc} = 0$ and Figure 6(b) corresponds to $\Delta_{rc} = 0.2$ mm. For both cases, from inlet-I, the tangential component of fluid's momentum is transported in the θ-direction along the shroud wall. For $\Delta_{rc} = 0.2$ mm, the large valued contour-band, starting from inlet-I, is extended almost up to inlet-II, whereas for $\Delta_{rc} = 0$, the large valued contour-band disappears well before inlet-II. Figure 7 shows the effect of radial
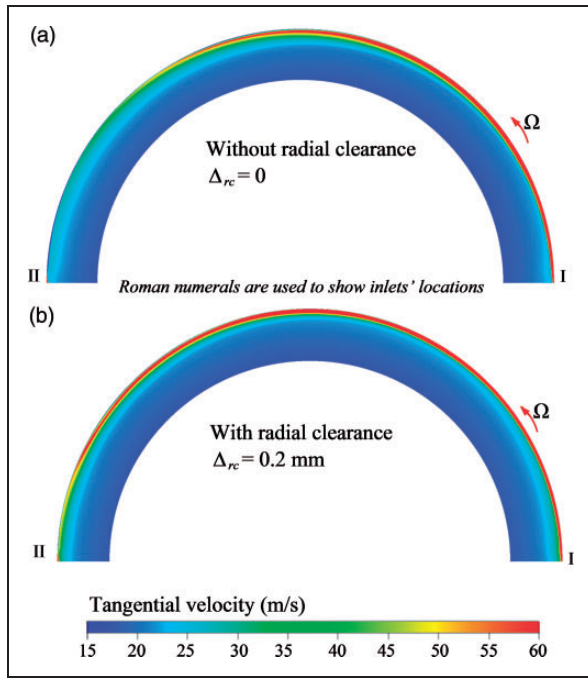
Figure 6. Effect of radial clearance on the distributions of tangential velocity near the inlet: (a) without radial clearance ($\Delta_{rc} = 0$); (b) with radial clearance ($\Delta_{rc} = 0.2$ mm). (For $N_{nozzle} = 2$, $d_t/b = 0$, $\dot{m}_o = 30$ mg/s, $\Omega = 800$ rad/s, $\alpha_i = 6°$, $T_{t,i} = 313$ K.)
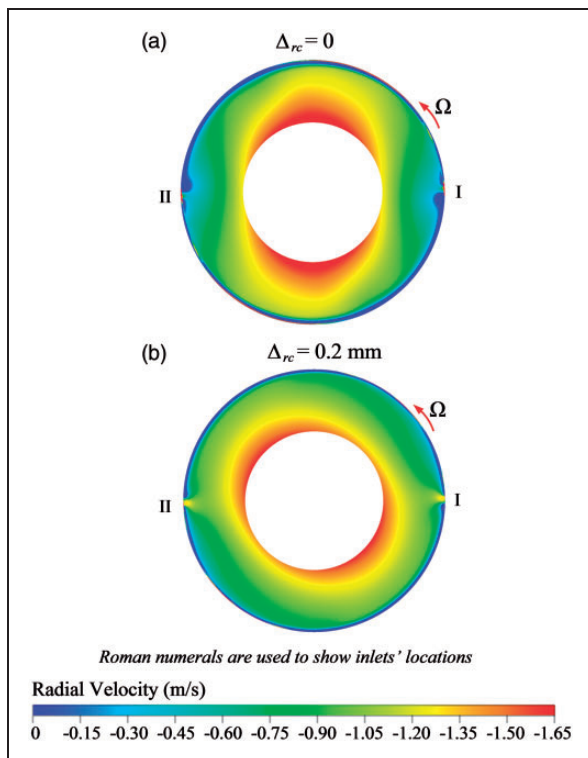
clearance on the distributions of radial velocity. Figure 7(a) corresponds to $\Delta_{rc} = 0$ and Figure 7(b) corresponds to $\Delta_{rc} = 0.2$ mm. For $\Delta_{rc} = 0$, the radial velocity (U_r) is typically nonaxisymmetric near the outlet. The azimuthal location of the large-U_r-zone near the outlet is offset from the azimuthal location of inlet-I in the direction of disc rotation. High absolute tangential velocity near inlet-I drives the fluid in the direction of disc rotation, and the radial entry of the fluid into the inter-disc-spacing is affected by the distribution of absolute tangential velocity along the rotor's periphery. For $\Delta_{rc} = 0.2$ mm, it can be observed that the radial velocity is almost axisymmetric near the outlet. The axisymmetry of radial velocity near the outlet is attained due to the nearly axisymmetric distribution of absolute tangential velocity (Figure 6(b)) along the rotor's periphery.

In brief, an increase in the radial clearance Δ_{rc} from zero to a finite value assists in the attainment of axisymmetric condition for both tangential and radial velocities, i.e. the axisymmetry is obtained at a larger radial location. With suitable combinations of N_{nozzle}, Ω, and Δ_{rc}, the axisymmetry in absolute tangential velocity may be obtained quite close to the inlet itself, whereas the nonaxisymmetry in radial velocity persists much longer along the flow path and axisymmetry is approached (for the adopted geometry) only near the outlet, if at all.

Role of the disc thickness (d_t)

This section investigates the effect of finite disc thickness (d_t) on the flow field. Results are shown for an 8-inlet configuration. The azimuthal extent covered by each inlet is 4°. Consider one such inlet spanning $-2° \leqslant \theta \leqslant 2°$. Figure 8 shows the contours of U_r and U_θ on a $r - z$ plane located at $\theta = 0°$ for $d_t/b = 1$ (for full admission). The contours display the spatial changes of the velocity components in the proximity of the inlet opening. Since the disc is rotating at a finite Ω, the value of U_θ is moderate on the disc's flat surfaces and edges (due to no-slip boundary condition). On the other hand, U_r is zero both at the disc's edge (due to no penetration boundary condition) and on the disc's flat surface (due to no-slip boundary condition). Both U_r and U_θ are large at the inlet opening. Beyond the radial-clearance space, fluid enters into the inter-disc-gap, and then, both U_r and U_θ decrease. From the two-dimensional $r - z$ plane, it may appear that U_r should increase instead of decreasing since the axial extent of the inlet opening $(b + d_t)$ is more than that of the inter-disc-spacing b. However, the total cross-sectional area of the eight discrete inlet openings is less than the cross-sectional area of the circumferential plane encompassing the rotor discs i.e. $2\pi r_d b$. Therefore, in order to explain the decrease of U_r and U_θ beyond the radial clearance space, the full three-dimensionality of the flow field should be taken into account.
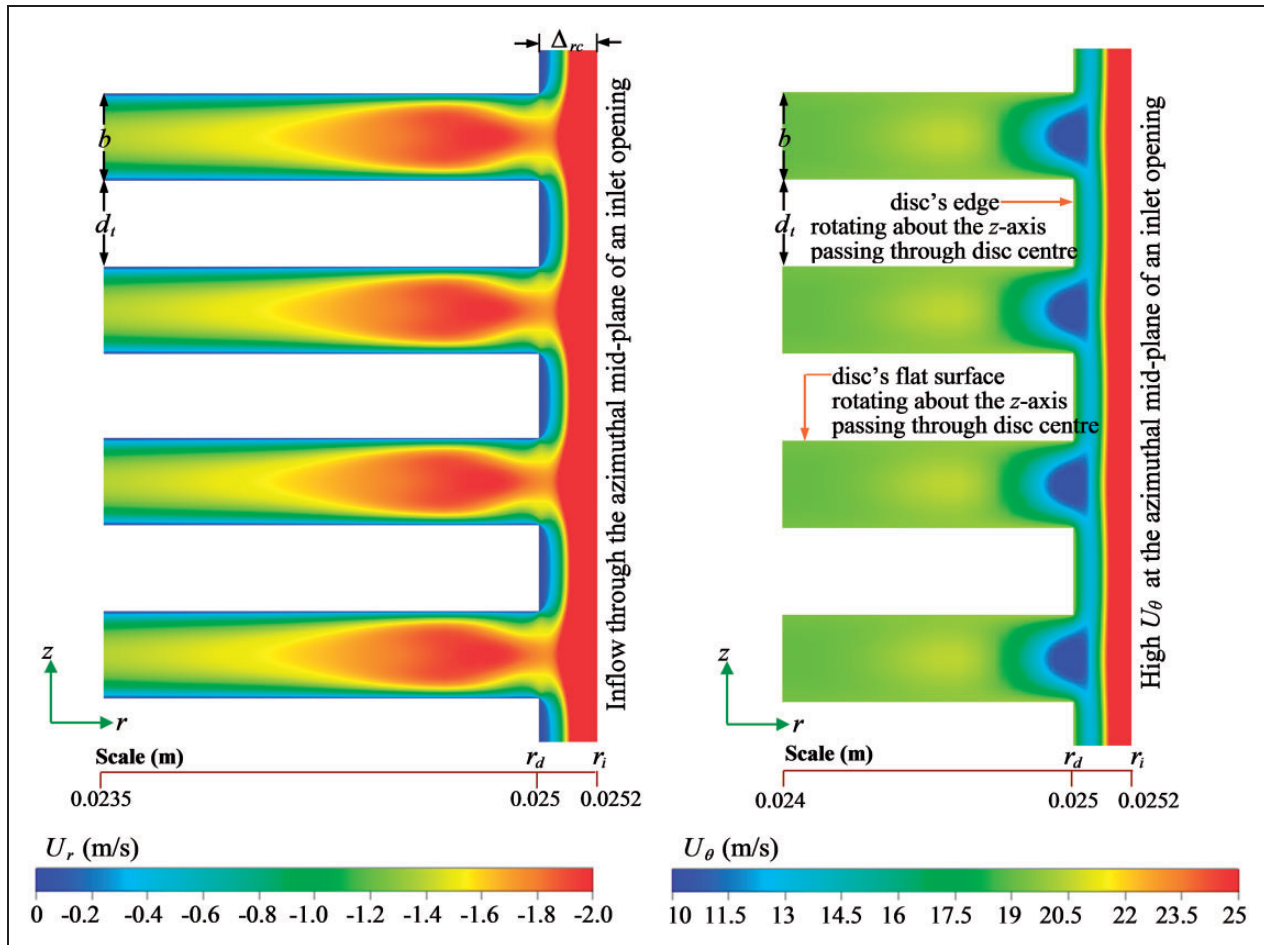

Figure 7. Effect of radial clearance on the distributions of radial velocity: (a) without radial clearance ($\Delta_{rc} = 0$); (b) with radial clearance ($\Delta_{rc} = 0.2$ mm). (For $N_{nozzle} = 2$, $d_t/b = 0$, $\dot{m}_o = 30$ mg/s, $\Omega = 800$ rad/s, $\alpha_i = 6°$, $T_{t,i} = 313$ K.)

Figure 8. Distributions of radial velocity (U_r) and absolute tangential velocity (U_θ) on a $r - z$ plane in the proximity of an inlet opening for finite disc thickness (d_t). (For $N_{nozzle} = 8$, $d_t/b = 1$, $\dot{m}_o = 30$ mg/s, $\Omega = 800$ rad/s, $\alpha_i = 6°$, $T_{t,i} = 313$ K, $\Delta_{rc} = 0.2$ mm. The upper end of the scale for the contours is restricted for revealing finer flow features elsewhere in the diagrams.)

Two consecutive inlets positioned at $-2° \leqslant \theta \leqslant 2°$ and $43° \leqslant \theta \leqslant 47°$ are separated by a part of the stationary shroud wall covering an azimuthal span $2° < \theta < 43°$. Nine representative $r - z$ planes are selected within the azimuthal span $-2° \leqslant \theta \leqslant 43°$ to depict the three-dimensional flow field. Figure 9 displays the contours of U_r and U_θ on these nine planes elucidating the changes of U_r and U_θ simultaneously in the r, θ and z directions. At $r = r_i$, a uniform mass distribution is set within the span $-2° \leqslant \theta \leqslant 2°$. However, the figure shows that at $r = r_d$, U_r becomes nonuniform within $-2° \leqslant \theta \leqslant 2°$, where, $U_r|_{\theta=2°}$ is much greater than $U_r|_{\theta=0°}$. This happens owing to the fluid's azimuthal spreading in the direction of disc rotation. At $r = r_i$, U_θ is large in the span $-2° \leqslant \theta \leqslant 2°$ because of the positioning of the inlets. The entire span $-2° \leqslant \theta \leqslant 2°$ at $r = r_d$, however, does not represent the location of large U_θ; in fact Figure 8 shows that U_θ (at $r = r_d$) is rather small at $\theta = 0°$. Figure 9 shows that U_θ at rotor inlet ($r = r_d$) becomes significantly large between $\theta = 2°$ and $\theta = 10°$; this shift is caused by the small angle (with the tangential direction) of fluid injection and the direction of disc rotation.

A few other observations from Figure 9 are as follows: (i) In the proximity of the inlet, a greater value of U_r is obtained within $0° < \theta < 10°$, whereas U_r is small beyond $\theta = 20°$. (ii) The U_θ-contours at $\theta = -2°$, $\theta = 0°$, and $\theta = 2°$ show that U_θ is large at the right most side of the $r - z$ plane indicating the location of the inlet opening. For $2° < \theta < 43°$, U_θ is zero at the right most side of the $r - z$ plane because of the specified no-slip condition on the stationary wall of the shroud. (iii) Within $5° < \theta < 20°$, the boundary layer near the shroud-wall grows, and, the large-U_θ-zone is shifted (radially inward) towards the inter-disc space. (iv) The large U_θ decreases in the θ-direction (see the contours at $\theta = 20°$, $\theta = 30°$, and $\theta = 40°$) to overcome the friction due to the stationary shroud and rotating discs.

Figure 10 shows the effect of increasing disc thickness d_t while the other input parameters (including the inter-disc-spacing b) are kept fixed. Representative results are shown for $d_t/b = 0$, $d_t/b = 1$ and $d_t/b = 2$. For all three cases, fluid injected from an inlet opening enters into the inter-disc space at r_d passing through the small radial clearance space. The cross-sectional area of the circumferential plane at r_d
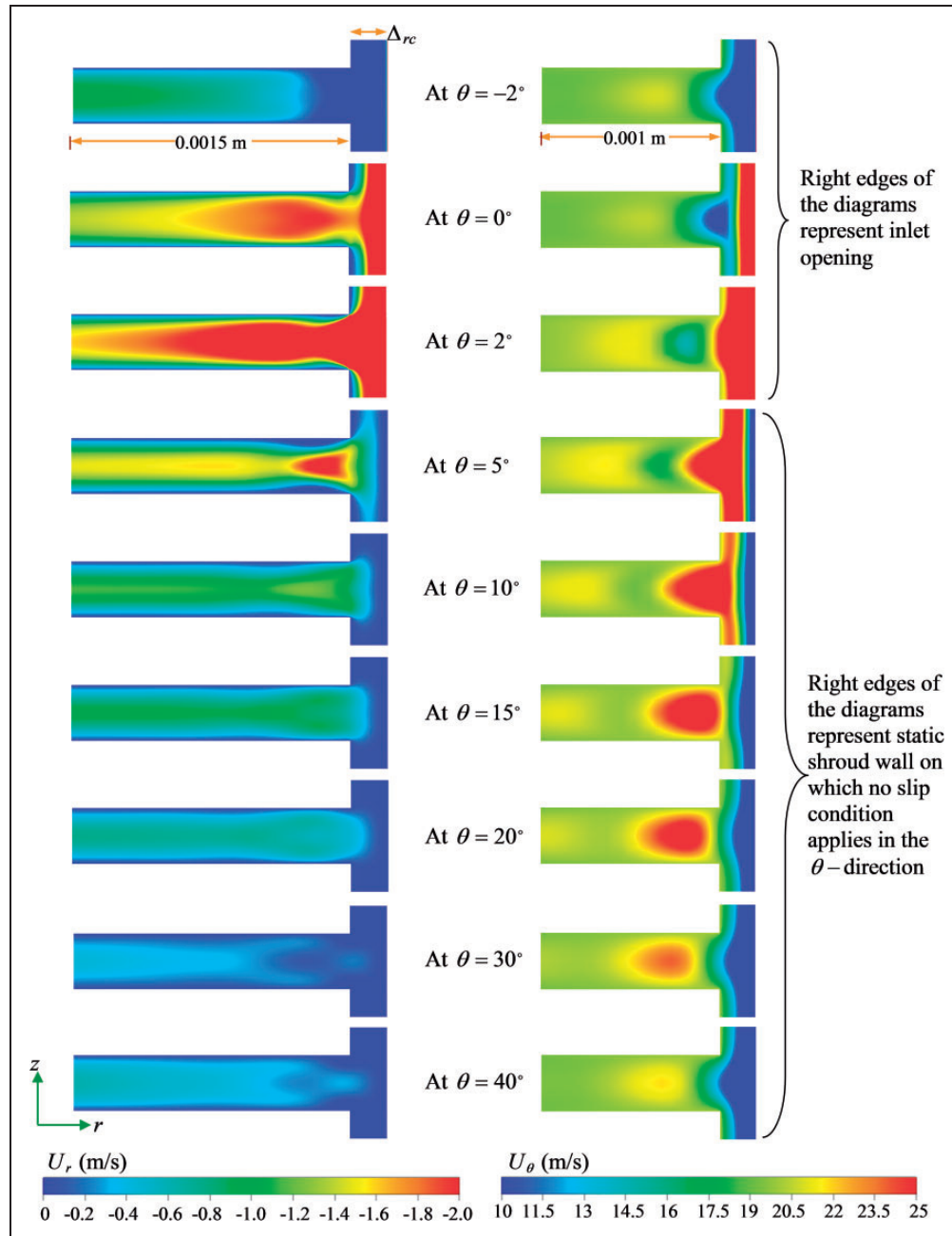
Figure 9. Distributions of radial velocity (U_r) and absolute tangential velocity (U_θ) on various $r - z$ planes between two consecutive inlet openings for finite disc thickness (d_t). (For $N_{nozzle} = 8$, $d_t/b = 1$, $\dot{m}_o = 30$ mg/s, $\Omega = 800$ rad/s, $\alpha_i = 6°$, $T_{t,i} = 313$ K, $\Delta_{rc} = 0.2$ mm. The upper end of the scale for the contours is restricted for revealing finer flow features elsewhere in the diagrams.)

is $2\pi b\, r_d$ which is independent of d_t. However, the cross-sectional area of the inlet opening is directly proportional to d_t. Since mass flow rate is the same for all three cases, the average radial velocity at the inlet opening ($U_{r,i}$) would decrease with increasing d_t. At the same time, $U_{\theta,i}$ would also decrease because the nozzle angle at the inlet is fixed. At $r = r_d$, although the area-averaged $\bar{U}_{r,d}$ is the same for all d_t/b, the local values of U_r on the circumferential plane may be very different owing to the simultaneous decrease of $U_{r,i}$ and $U_{\theta,i}$ with increasing d_t/b. The contour plots in the figure show how the qualitative trend changes

with d_t. In order to reveal the quantitative details at $r = r_d$, the z-profiles of U_r are also plotted for various d_t/b. Figure 10 shows that when the value of d_t/b is increased from 0 to 1, the z-profile of U_r at $\theta = 0°$ changes from W-shaped to nearly parabolic; and when d_t/b is increased from 1 to 2, the nearly parabolic distribution becomes more peaky.

Vectors are overlaid on the contours to indicate the direction of fluid flow on the $r - z$ planes. It is to be noted that these vectors possess only two components, namely U_r and U_z. The effect of U_z is noticeable in the radial clearance space. U_z decreases rapidly within
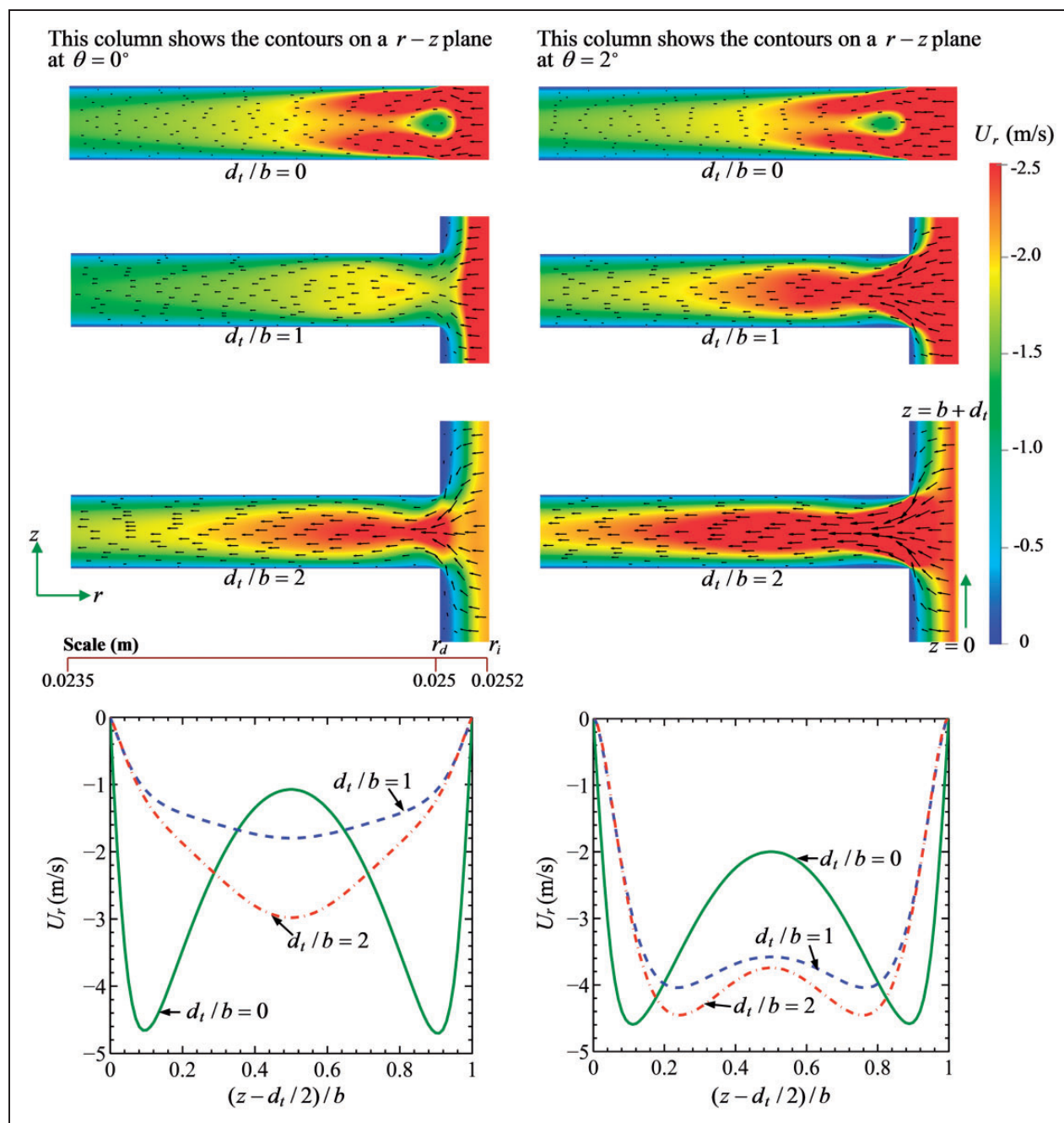
Figure 10. Role of disc thickness on the distribution of radial velocity (U_r) in the proximity of an inlet opening. (For $N_{nozzle} = 8$, $\dot{m}_o = 30$ mg/s, $\Omega = 800$ rad/s, $\alpha_i = 6°$, $T_{t,i} = 313$ K, $\Delta_{rc} = 0.2$ mm. The upper end of the scale for the contours is restricted for revealing finer flow features elsewhere in the diagrams.)

a short radial distance in the downstream direction from $r = r_d$.

Implications of the nozzle–rotor interaction on the turbine performance

In the previous section, we elucidated the detailed fluid dynamics of the nozzle-rotor interaction arising out of a finite number of discrete nozzles, a finite radial clearance between the rotor and shroud wall, and a finite thickness of the discs. The fluid dynamics is important from a fundamental viewpoint. It is also

intimately linked with the energetics of the rotor assembly. When considered as an engineering device, the success of the Tesla disc turbine must be assessed by its performance characteristics. This section therefore presents a comprehensive study of the dependence of turbine performance on various parameters of nozzle–rotor interaction, namely N_{nozzle}, Ω, Δ_{rc}, and d_t. The three important performance parameters are power input, power output, and efficiency. From the available definitions of efficiency (η) for a Tesla turbine,[16] the following definition of efficiency is adopted here for the

numerical illustrations

$$\eta = \frac{\dot{W}}{\sum\limits_{j=1}^{N_{nozzle}} Q_j p_{t,j}}. \qquad (8)$$

The denominator of equation (8) signifies the power input per channel. For any flow configuration, N_{nozzle} is the number of discrete inlets, Q_j is the rate of volume inflow through jth inlet per rotating channel, and $p_{t,j}$ is the mass-flow-averaged total pressure at the jth inlet. The mass flow rate through the outlet per rotating channel $\dot{m}_o$ is therefore connected, under steady flow condition, to Q_j through the relation $\dot{m}_o = \rho_i \sum_{j=1}^{N_{nozzle}} Q_j$, where ρ_i is the fluid density at the inlet (at $r = r_i$) $\dot{W}$ in the numerator of equation (8) indicates the net power output obtained from a single rotating channel. When the disc thickness d_t is zero, the torque and power are produced on the two (flat) disc surfaces that constitute a rotating channel. When d_t is nonzero, the circumferential surfaces (i.e. the disc edges at inlet and outlet) also contribute to the torque and power; under certain operating conditions this component of torque and power may be negative. If the net torque per rotating channel is Γ and the rotational speed of the discs is Ω, then the power output per channel ($\dot{W}$) would be equal to $\Gamma\Omega$. (For a particular Ω, Γ is obtained from the present CFD simulations.)

In order to extract the physics of power production from a systematic parametric study, each of the four parameters N_{nozzle}, Ω, Δ_{rc}, and d_t is varied individually while keeping the others fixed at some representative values. The disc thickness d_t is assumed zero in the first part of the parametric analysis in which the effects of N_{nozzle}, Ω, Δ_{rc} are established. The disc thickness d_t is varied in the second part of the parametric analysis. The effects of varying the shape of the disc-edge are also then determined. Additionally, the effects of partial or full admission (i.e. the effects of varying the axial extent of nozzle openings) are also studied here.

It should be appreciated that for each combination of N_{nozzle}, Ω, Δ_{rc}, and d_t, a fully three-dimensional CFD simulation needed to be performed on a fine grid necessary to capture the fluid dynamics at a small scale inside the clearance space (see Table 2 for the total number of computational cells which exceeds 10 million for certain simulations). Each discrete point shown in the next few figures represents one such simulation. In order to capture the physics thoroughly, a very large number of separate, fully three-dimensional, CFD simulations are therefore performed (about 150 are performed, out of which results of 100 selected simulations are shown in the next seven performance curves). Each CFD simulation is run to a high degree of convergence (maximum RMS residual being 10^{-6}). The CPU time for each
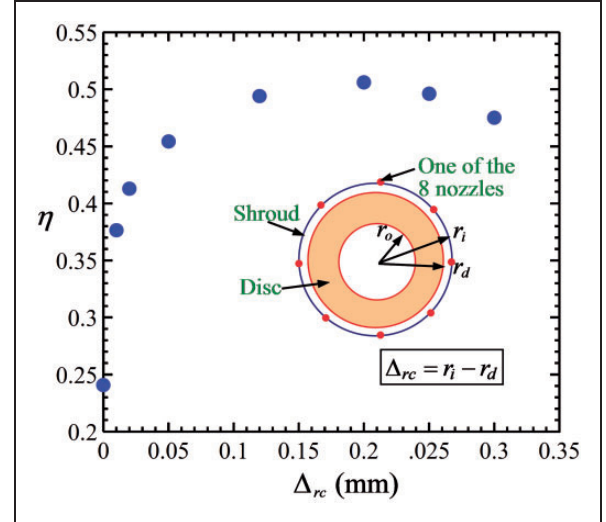

Figure 11. Effect of radial clearance (Δ_{rc}) on the efficiency (η) of the turbine. (For $N_{nozzle} = 8$, $d_t/b = 0$, $\dot{m}_o = 30$ mg/s, $\Omega = 1500$ rad/s, $\alpha_i = 6°$, $T_{t,i} = 313$ K. Each symbol represents the result of a separate three-dimensional CFD simulation.)

simulation varied from about 4 h to about 32 h, run on a cluster (x86-64 architecture and 198 GB RAM) of 16 processors (Intel(R) Xeon(R) CPU E5-4640 with base frequency of 2.40 GHz). Such a comprehensive set of high-precision, fully three-dimensional (nonaxisymmetric) resource-intensive computations has never been attempted in the past.

At first, we investigate the effect of varying the radial clearance Δ_{rc} on the efficiency of a Tesla disc turbine. The investigation is performed for an 8-inlet configuration ($N_{nozzle} = 8$) keeping $\dot{m}_o$, α_i and $T_{t,i}$ fixed. Figure 11 shows the results of CFD simulations obtained by varying Δ_{rc} from zero to a sufficiently large finite value. It can be seen that the efficiency is small when Δ_{rc} is zero. With increasing Δ_{rc} the efficiency increases rapidly, and a maximum value of efficiency is attained at a certain value of Δ_{rc} (i.e. 0.2 mm in the present case). Any further increase in Δ_{rc} leads to a decrease in efficiency (however, this decrease occurs at a much slower rate). The above observations can be explained in following way. The torque is proportional to r^3.[19] Therefore, a significant portion of the total torque is generated on the flat disc surfaces in the region near the outer radius of the disc (r_d). At the shroud-wall, the tangential velocity is brought to zero due to the no-slip boundary condition. When the radial clearance is small, the boundary layer developed due to the stationary shroud-wall overlaps with the large toque producing region (inside the rotating channel); and, a large amount of angular momentum is lost to withstand the friction within the boundary layer. When the radial clearance is large, the presence of a thick (nearly) stagnant layer of fluid adjacent to the stationary shroud is responsible for a reduction in the fluid's absolute tangential velocity along the rotor's periphery. For this reason,

the inlet condition becomes inefficient. Therefore, an optimum Δ_{rc} exists for which the efficiency is the maximum.

A quantitative indication of the above-mentioned physics may be obtained as follows. For an 8-nozzle configuration with $\dot{m}_o = 3 \times 10^{-5}$ kg/s and full admission, the values of tangential and radial velocities at the nozzle openings (at $r = r_i$) are $U_\theta = 58.42$ m/s and $U_r = -6.14$ m/s, and the nozzle angle is set at $\alpha_i = 6°$. For steady flow with a fixed $\dot{m}_o$, the average radial velocity $\bar{U}_{r,d}$ at the rotor inlet (i.e. at $r = r_d$) is fixed. The average tangential velocity $\bar{U}_{\theta,d}$, however, is altered due to the no-slip condition on the shroud wall and the presence of the fluid mass in the clearance space. The effective inflow angle at rotor inlet, $\bar{\alpha}_d$, where $\bar{\alpha}_d = \tan^{-1}(|\bar{U}_{r,d}|/\bar{U}_{\theta,d})$, therefore decreases as $\bar{U}_{\theta,d}$ increases and vice versa. It is shown in Guha and Sengupta,[2] that the efficiency increases with decreasing $\bar{\alpha}_d$ (which was obtained in Guha and Sengupta[2] by increasing $\bar{U}_{\theta,d}$ for a fixed $\bar{U}_{r,d}$). Therefore, with varying radial clearance Δ_{rc}, the efficiency of the turbine changes as $\bar{U}_{\theta,d}$ and $\bar{\alpha}_d$ change. In order to obtain a quantitative feeling, the results of the CFD simulations are post-processed to numerically determine the values of $\bar{U}_{\theta,d}$ and $\bar{\alpha}_d$ (averaged over the circumferential area $2\pi r_d b$) for various values of Δ_{rc}. Table 3 shows the outcome. It is found that when $\Delta_{rc} = 0$, the no-slip condition on the shroud wall has the maximum influence and a very low value of $\bar{U}_{\theta,d}$ is obtained. As Δ_{rc} is progressively increased, the shroud surface moves away from the rotor periphery. There is thus a rapid increase in $\bar{U}_{\theta,d}$ and a rapid decrease in the effective angle at rotor periphery $\bar{\alpha}_d$ (Table 3); thus the efficiency of the Tesla turbine increases significantly with increasing Δ_{rc} (Figure 11). After a certain value of Δ_{rc}, however, $\bar{U}_{\theta,d}$ starts decreasing slowly (and $\bar{\alpha}_d$ increases slowly) with any further increase in Δ_{rc} (Table 3). Consequently, the efficiency versus radial clearance curve shows a maxima (Figure 11). The shroud wall is then

Table 3. Variations of averaged flow quantities at the rotor inlet (at $r = r_d$) with radial clearance (Δ_{rc}) (for $N_{nozzle} = 8$, $d_t/b = 0$, $\dot{m}_o = 30$ mg/s, $\Omega = 1500$ rad/s, $\alpha_i = 6°$, $T_{t,i} = 313$ K).

Δ_{rc} (mm)	$\bar{U}_{\theta,d}$ (m/s)	$\bar{U}_{r,d}$ (m/s)	$\bar{\alpha}_d$ (degree)
0	5.32	−0.56	6.00
0.01	13.25	−0.56	2.42
0.02	19.30	−0.56	1.66
0.05	32.68	−0.56	0.98
0.10	41.66	−0.56	0.77
0.20	46.78	−0.56	0.69
0.25	45.89	−0.56	0.70
0.30	43.65	−0.56	0.73
0.35	42.44	−0.56	0.76

sufficiently far away such that any effect due to its further receding is not significant, but the loss in the increasing volume of the slowly rotating fluid in the clearance space increases.

A large number of CFD simulations are performed for various combinations of N_{nozzle} and Ω keeping $\dot{m}_o$, α_i, $T_{t,i}$, and Δ_{rc} fixed. The compressible version of the flow equations is solved. The density distribution in the flow field, and the change in static pressure between radius r_i and r_o are obtained from the flow solutions. The computed density at inlet fixes the volume flow rate Q_j. With the static pressure prescribed at the outlet and the computed difference in static pressure, the total pressure $p_{t,j}$ at inlet can be determined. The torque Γ produced per rotating channel can be computed directly from the flow solution. All quantities in equation (8) are then known. In this way, the power input per channel, power output per channel and efficiency are calculated for each CFD simulation. Results are displayed in Figures 12 and 13. Figure 12 shows that with increasing Ω, the power input per channel increases. The power input per channel increases because of the increase in the overall pressure drop Δp_{io} which is mainly attributed to the fact that the centrifugal component of the overall pressure drop increases with increasing Ω.[20] The power output per channel ($\dot{W}$) versus Ω curves (Figure 12), for each fixed value of N_{nozzle}, are of the shape of an inverted bucket. The existence of the optimum values of Ω for maximum $\dot{W}$ can be explained from a simple theory. It has been postulated in Hoya and Guha[16] and demonstrated in Guha and Sengupta[2] that $\Gamma \approx c_1 - c_2\Omega$. Therefore, $\dot{W} = \Gamma\Omega = c_1\Omega - c_2\Omega^2$. The optimum Ω for maximum power output is therefore obtained by setting $\partial\dot{W}/\partial\Omega = 0$. This gives, $\Omega_{\text{max power}} = c_1/2c_2$.

Figure 13 show that the η versus Ω curves, for each fixed value of N_{nozzle}, are of the shape of an inverted bucket. This establishes a quantitative relation between the number of nozzles and the corresponding best rotational speed of the rotor. It is also established that as the number of nozzles is increased, the operable range of Ω decreases, the buckets become more peaky and the maximum possible efficiency increases. The η versus Ω curves are inverted bucket shaped due to the following reason. It is already established that the variation of output power $\dot{W}$ with rotational speed Ω shows the shape of an inverted bucket since $\dot{W} = \Gamma\Omega = c_1\Omega - c_2\Omega^2$. Since the overall pressure drop between the inlet and the outlet Δp_{io} changes mainly because of the centrifugal component at high Ω, the pressure drop would be approximately given by $\Delta p_{io} \approx c_3 + c_4\Omega^2$.[20] The magnitude of Δp_{io} determines the power input. It is already mentioned that the turbine efficiency η is the ratio of the power output per channel to the power input per channel. Thus, with increasing Ω, the efficiency first increases due to the increase in power output, but eventually decreases because of the combined effect of the decrease
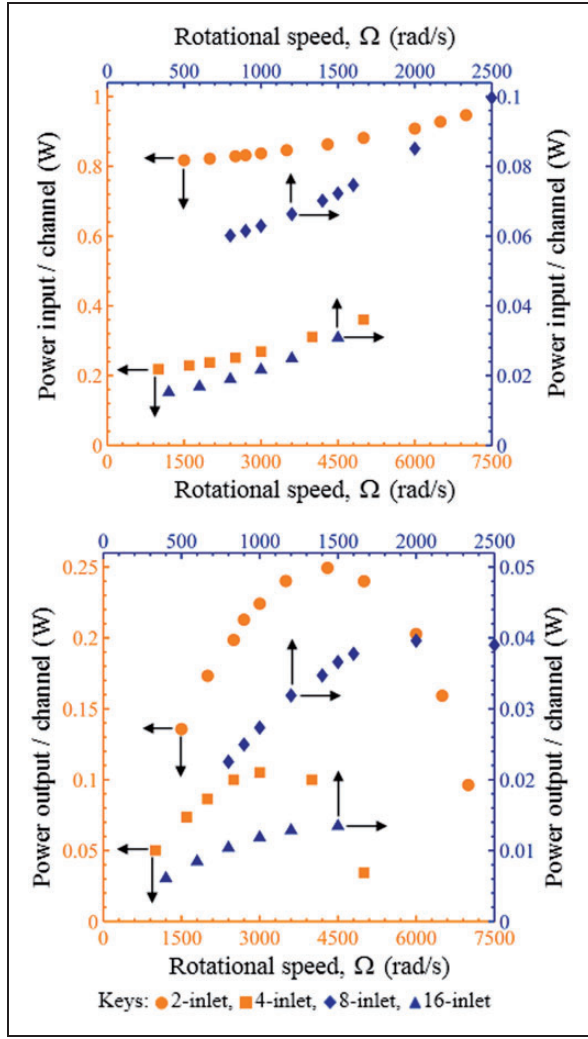
Figure 12. Variations in power input and power output per rotating channel with rotational speed: the effect of varying the number of inlet-nozzles. (For $\dot{m}_o = 30$ mg/s, $d_t/b = 0$, $\alpha_i = 6°$, $T_{t,i} = 313$ K, $\Delta_{rc} = 0.2$ mm. The left and bottom axes correspond to 2-inlet and 4-inlet configurations; and, the right and top axes correspond to 8-inlet and 16-inlet configurations (the arrows are inserted in order to indicate the appropriate axes for any configuration). Each symbol represents the result of a separate three-dimensional CFD simulation.)

in power output and the increase in overall pressure drop which increases the power input. For maximum η, $\partial\eta/\partial\Omega = 0$. Substitution of the mathematical expressions for power output and power input in the condition for maximum efficiency sets the optimum value of rotational speed, $\Omega_{\max\eta}$. When this algebra is carried out, it is found that $\Omega_{\max\eta} = \frac{ac}{b}\left[\sqrt{1 + \frac{b}{a^2 c}} - 1\right]$, where $a = c_2/c_1$, $b = c_4/c_1$, $c = [c_3 + 0.5\rho(\bar{U}_{\theta,d}^2 + \bar{U}_{r,d}^2)]/c_1$.

Figure 13 exhibits that when N_{nozzle} is increased from 2 to 16, the peak value of efficiency is increased by nearly a factor of 2. The present comprehensive study thus demonstrates quantitatively, for the first time, that an axisymmetric inflow condition along
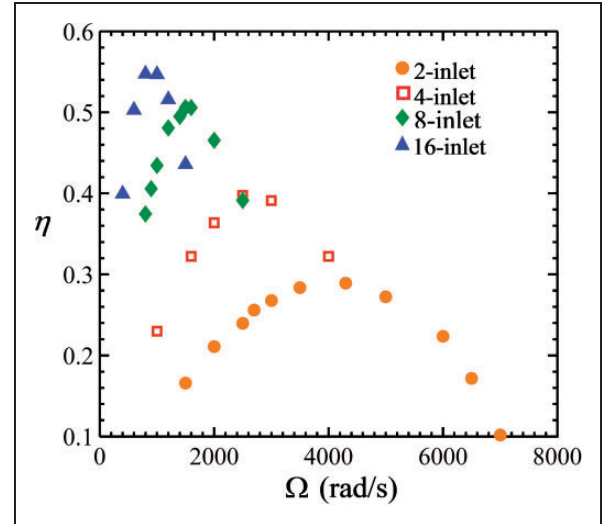

Figure 13. Variation of efficiency (η) with rotational speed (Ω): the effect of varying the number of inlet-nozzles. (For $\dot{m}_o = 30$ mg/s, $d_t/b = 0$, $\alpha_i = 6°$, $T_{t,i} = 313$ K, $\Delta_{rc} = 0.2$ mm. Each symbol represents the result of a separate three-dimensional CFD simulation.)

the rotor's periphery ensures the best possible design for an efficient rotor.

It is already established that flow axisymmetry is achieved at a greater radius (i.e. closer to the rotor inlet) when N_{nozzle} is increased. It is therefore interesting to examine whether one may attain the performance of the rotor for an axisymmetric inflow configuration by using a large number of discrete inflows. Table 4 shows such a comparison for a non-axisymmetric inflow configuration having $N_{nozzle} = 16$ at various values of rotational speed Ω. The power outputs for the axisymmetric inflow configuration, given in Table 4, are determined by the analytical theory developed in Sengupta and Guha.[23] Table 4 shows that the power outputs for $N_{nozzle} = 16$ are quite close to those for the axisymmetric configuration, particularly when Ω is not large. The trend of results displayed in Figure 13 suggests that the non-axisymmetric power output will approach closer to the axisymmetric case as N_{nozzle} is increased further.

So far in this section, we have neglected the presence of the disc thickness. For a nonzero disc thickness, the torque on the circumferential surfaces (i.e. the disc edges) needs to be considered in addition to the torque on the flat disc surfaces. Under efficient operating conditions, the torque produced by the inner circumferential surfaces would be much smaller than the torque produced by the outer circumferential surfaces.[19] This is so because the outer surface of a disc is located at a greater radius (where velocity gradient is expected to be greater) and the surface area of the outer surface is greater than the inner surface. The effect of finite disc thickness (d_t) is first studied for straight disc edge with the inlet openings spanning over the entire axial extent of the Tesla disc turbine for an 8-inlet configuration. The variation of η with Ω

Table 4. A comparison of power output obtained by the CFD simulations for $N_{nozzle} = 16$ with the prediction of the analytical theory[23] for axisymmetric inflow configuration (for radius ratio $(\equiv r_o/r_d) = 0.528$, aspect ratio $(\equiv b/r_d) = 0.012$, dynamic similarity number at r_d $(\equiv (b/r_d)(|\bar{U}_{r,d}|b/\nu)) = 0.125$).

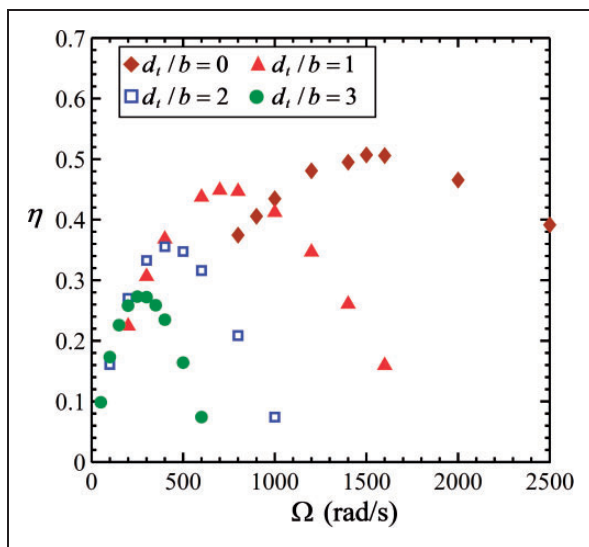| | | | Nondimensional power output/ disc surface $\dot{W}/(2\rho|U_{r,d}|^3 r_d^2)$ | |
| | | | Analytical theory | |
Ω (rad/s)	Tangential speed ratio at r_d $(\equiv \bar{U}_{\theta,d}/\Omega r_d)$	Flow angle at r_d in degree $(\equiv \tan^{-1}\frac{|\bar{U}_{r,d}|}{\bar{U}_{\theta,d}})$	(for axisymmetric inflow configuration)	CFD simulations (for 16-inlet configuration)
400	2.179	1.48	25.07	24.11
600	1.519	1.42	35.24	33.48
800	1.190	1.36	43.90	41.08
1000	0.996	1.30	51.33	46.89

Figure 14. Variation of efficiency (η) with rotational speed (Ω): the effect of varying the disc thickness. (For $N_{nozzle} = 8$, $\dot{m}_o = 30$ mg/s, $\alpha_i = 6°$, $T_{t,i} = 313$ K, $\Delta_{rc} = 0.2$ mm. Each symbol represents the result of a separate three-dimensional CFD simulation.)
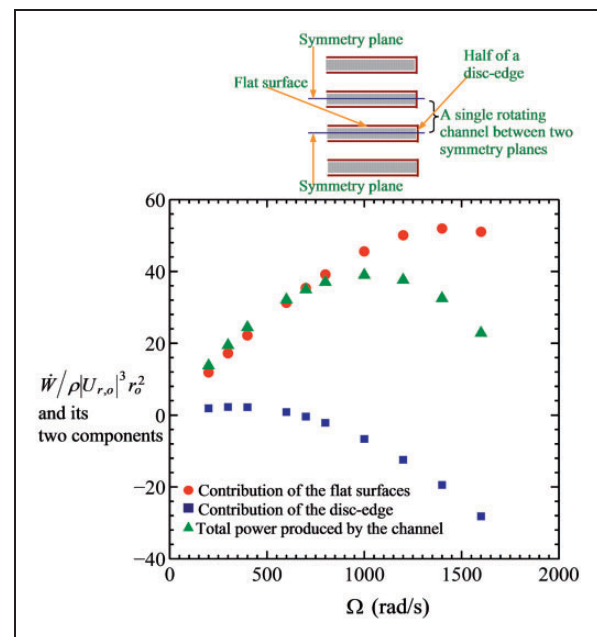

Figure 15. Contributions of disc edge and disc's flat surfaces in the production of the total output power by a single rotating channel. (For $N_{nozzle} = 8$, $d_t/b = 1$, $\dot{m}_o = 30$ mg/s, $\alpha_i = 6°$, $T_{t,i} = 313$ K, $\Delta_{rc} = 0.2$ mm. Each symbol represents the result of a separate three-dimensional CFD simulation.)

is determined for various values of d_t while all other input parameters are kept fixed. Figure 14 shows that the η versus Ω curves are of the shape of an inverted bucket. For each curve, the maximum value of η occurs at a certain value of Ω. For the ease of discussion, we denote the maximum η by η_{max} and the corresponding Ω by $\Omega_{max\,\eta}$. The figure shows the decrease of both η_{max} and $\Omega_{max\,\eta}$ with increasing d_t. When d_t increases, the decrease of power output is more than the decrease of power input; therefore, η_{max}, the ratio of power output to power input, decreases. We now explain why $\Omega_{max\,\eta}$ also decreases with an increase in d_t. Figure 12 shows that the power output ($\dot{W}$) versus Ω curves are of the shape of an inverted bucket exhibiting maxima whereas the curves corresponding to power input decreases monotonically with decreasing Ω. With increasing d_t, the Ω, for which the maximum value of $\dot{W}$ occurs, decreases. As a result, $\Omega_{max\,\eta}$

also decreases with increasing d_t. (From the fluid dynamic point of view, it is established here that the condition $d_t/b \rightarrow 0$ is desirable since it maximizes the efficiency, but, in a real design, the strength aspects also need to be taken into consideration.)

When d_t is zero, the power is solely produced by the disc's flat surfaces. For a nonzero d_t, the power is partly produced by the flat surfaces and partly by the disc edge. Figure 15 displays the variations of total power output and its two components with Ω while all other input parameters are kept fixed. The figure shows that the power produced by flat surfaces is much greater than the power produced by disc edge. Beyond a certain value of Ω, the disc edge, instead of producing power, would absorb power (indicated by the negative sign of this component in the graph).
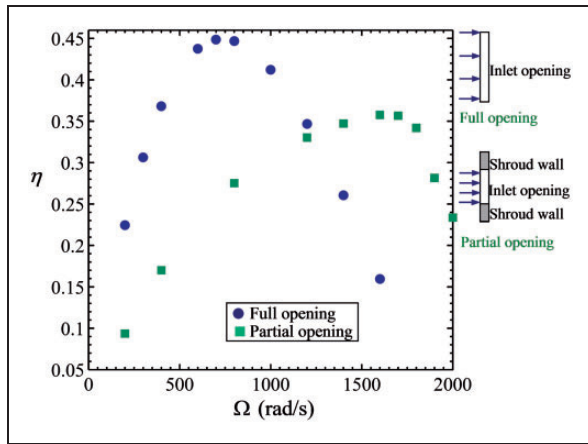
Figure 16. Variation of efficiency (η) with rotational speed (Ω): full opening versus partial opening. (For $N_{nozzle} = 8$, $d_t/b = 1$, $\dot{m}_o = 30$ mg/s, $\alpha_i = 6°$, $T_{t,i} = 313$ K, $\Delta_{rc} = 0.2$ mm. Each symbol represents the result of a separate three-dimensional CFD simulation.)
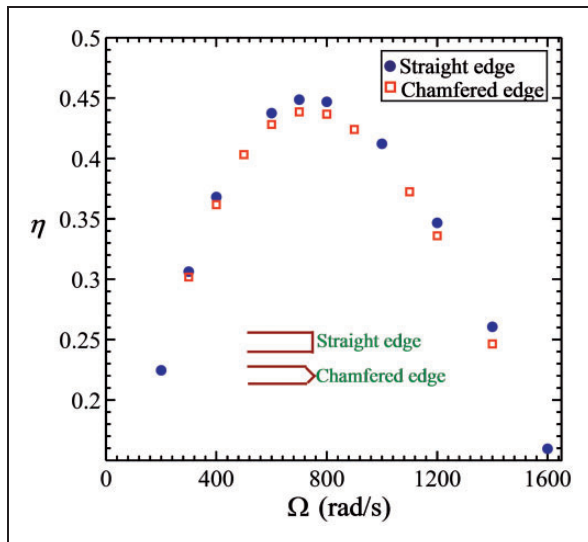

Figure 17. Variation of efficiency (η) with rotational speed (Ω): straight edge versus chamfered edge. (For $N_{nozzle} = 8$, $d_t/b = 1$, $\dot{m}_o = 30$ mg/s, $\alpha_i = 6°$, $T_{t,i} = 313$ K, $\Delta_{rc} = 0.2$ mm. Each symbol represents the result of a separate three-dimensional CFD simulation.)

With increasing Ω, the magnitude of the absorbed power increases. Moreover, the power produced by the flat surfaces decreases beyond a certain value of Ω. These two effects together result into a decrease of total power output above a certain value of Ω.

Now we elucidate a subtle modification of the inlet-opening and its effect on the efficiency of a Tesla disc turbine. One may hypothesize that a jet-like inflow hitting directly the solid edges of the discs would be wasteful and thus an improved design would be to use partial admission of the fluid through the shroud. Instead of being continuous in the direction parallel to the rotor axis, each nozzle would produce $n_d - 1$

number of discrete jets (where n_d is the number of discs), punctuated by gaps whose thickness matches with the thickness of each disc, hoping that in this way the inflow can effectively be directed only through the inter-disc spacings. Figure 16 compares η versus Ω curve for a full-opening configuration with that for a partial opening configuration. It can be observed that the maximum efficiency obtained from the partial opening configuration is less than that for the full-opening configuration. The reason for this is as follows. With the application of partial opening, the power output increases; however, the power input increases by a greater amount due to the large increase of the total pressure at the inlet (the study is conducted for constant values of $\dot{m}_o$ and N_{nozzle}).

Finally, we investigate the effect of contouring the edges of the discs (e.g. using a chamfered (tapered) tip) so that the generation of work-absorbing shear stress on the disc edges can be reduced, thereby improving the performance. Figure 17 shows the effect of chamfering the disc-edge. The chamfer is symmetric about the mid-plane of the disc and a chamfer angle of $45°$ is used. Chamfering is done such that the maximum outer radius of the disc remains the same as the outer radius of the straight edge disc i.e. r_d. Chamfering of the disc edge reduces the area of the disc's flat surfaces by a small amount near the outer periphery of the disc. The inclined surfaces there may produce power output but the effective inter-disc gap increases, thereby producing less shear stress than what would have been produced if the flat surfaces were maintained up to the outer radius of the disc (r_d). Since torque is proportional to r^3, a significant portion of the total torque is generated in the region near the outer radius of the disc (r_d). Thus, although the power absorbed by the disc-edge is decreased, chamfering reduces the total power output by a small amount. It is to be noted that the power input changes insignificantly as a result of chamfering and, hence, the efficiency decreases slightly as observed in the figure.

Conclusion

The present CFD study reveals the complex interaction of discrete multiple inflows with the stationary shroud and the rotating channels of a Tesla disc turbine, highlighting the dependence of the fluid dynamics and power transfer on four important input parameters, namely the number of nozzles (N_{nozzle}), rotational speed of the discs (Ω), radial clearance between the rotor and the shroud (Δ_{rc}), and disc thickness (d_t). The results are obtained for fixed values of mass flow rate, total temperature at inlet and flow angle at inlet. Detailed (computationally obtained) flow visualizations are constructed to illustrate the three-dimensional flow features generated by the presence of discrete inlets and finite thickness of the discs.

When the number of nozzles N_{nozzle} is increased, keeping all other input parameters fixed, the flow condition at the rotor's inlet becomes more uniform, which assists in the attainment of axisymmetric condition in the tangential and radial velocities, i.e. the axisymmetry is obtained at a larger radial location. The distributions of absolute tangential velocity U_θ and pressure within the inter-disc-spacing, as compared to the distribution of radial velocity (U_r) within the inter-disc-spacing, attain axisymmetry for smaller number of inlet nozzles.

When the rotational speed of the discs (Ω) is changed keeping all other input parameters fixed, the distribution of radial velocity is significantly altered, which may result even in a change of the fundamental shape of its z-profile. Thus with increasing Ω, the z-profile of radial velocity changes from parabolic to flat to W-shaped. This an important and interesting effect of Ω on the fundamental shape of the z-profile of U_r has not been described in the previous literature.

An increase in the radial clearance Δ_{rc} from zero to a finite value assists in the attainment of axisymmetric condition for both tangential and radial velocities, i.e. the axisymmetry is obtained at a larger radial location. With suitable combinations of N_{nozzle}, Ω, and Δ_{rc}, the axisymmetry in absolute tangential velocity may be obtained quite close to the inlet itself, whereas the non-axisymmetry in radial velocity persists much longer along the flow path and axisymmetry is approached (for the adopted geometry) only near the outlet, if at all.

The existence of an optimum Δ_{rc} is demonstrated here, for which the efficiency of the rotor is maximized (Figure 11). An explanation is provided in terms of the effective values of the tangential velocity $\bar{U}_{\theta,d}$ and flow angle $\bar{\alpha}_d$ at the rotor inlet. The study establishes quantitatively how the tangential velocity and flow angle at the outlet of discrete nozzles develop respectively into $\bar{U}_{\theta,d}$ and $\bar{\alpha}_d$ through the complex rotor-inflow interaction inside the small space provided by the radial clearance.

A large number of CFD simulations for various combinations of N_{nozzle} and Ω show that the η versus Ω curves (Figure 13), for each fixed value of N_{nozzle}, are of the shape of an inverted bucket. This establishes a quantitative relation between the number of nozzles and the corresponding best rotational speed of the rotor. It is also established that as the number of nozzles is increased, the operable range of Ω decreases, the buckets become more peaky and the maximum possible efficiency increases. The present comprehensive study thus demonstrates quantitatively, for the first time, that an axisymmetric inflow condition along the rotor's periphery ensures the best possible design for an efficient rotor.

It is found that the disc thickness (d_t) plays a critical role either in influencing the fluid dynamics or in determining the performance of Tesla turbines. When the disc thickness (d_t) is changed keeping all other input parameter fixed, the velocity field in the proximity of an inlet opening is changed significantly. Figure 10 shows that when the value of d_t/b is increased from 0 to 1, the $z-$ profile of U_r at $\theta = 0°$ changes from W-shaped to nearly parabolic; and when d_t/b is increased from 1 to 2, the nearly parabolic distribution becomes more peaky.

By combining the physical insight contained in Figures 11 to 17, the following design decisions may be formulated, which need to be combined with the optimization methodology given in Guha and Smiley[1] and Guha and Sengupta,[2] for designing an efficient Tesla disc turbine. Establishing axisymmetric boundary condition at the rotor outer periphery provides the highest possible efficiency. Axisymmetry may be approached by increasing the number of discrete nozzles (or by using a plenum chamber). It is shown that, when N_{nozzle} is increased from 2 to 16, the peak value of efficiency is increased by nearly a factor of 2 and the maxima occur at lower rotational speeds. As the disc thickness (d_t/b) is increased from the limiting value of zero to 3, the peak efficiency is shown to decrease by nearly a factor of 2 and the maxima occur at lower rotational speeds. The effects of a small number of inlets or a large disc thickness on the performance and efficiency of a Tesla disc turbine can thus be rather dramatic. It is further concluded that chamfering of the disc edge or partial admission decreases the turbine efficiency. Thus, small disc thickness, straight disc edge, full nozzle opening, optimum radial clearance, and inlet condition as close to axisymmetry as is possible are recommended for the design of an efficient Tesla disc turbine.

Declaration of Conflicting Interests

Funding

ORCID iD

Sayantan Sengupta ⓘ http://orcid.org/0000-0001-8470-2218.

References

1. Guha A and Smiley B. Experiment and analysis for an improved design of the inlet and nozzle in Tesla disc turbines. *Proc IMechE, Part A: J Power and Energy* 2010; 224: 261–277.
2. Guha A and Sengupta S. A non-dimensional study of the flow through co-rotating discs and performance optimization of a Tesla disc turbine. *Proc IMechE, Part A: J Power and Energy*, DOI: 10.1177/0957650 917715148.
3. Tesla N. *Turbine*. US Patent 1 061 206, 1913.
4. Guha A. Optimisation of aero gas turbine engines. *Aeronaut J* 2001; 105: 345–358.

5. Guha A. Performance and optimization of gas turbines with real gas effects. *Proc. IMechE, Part A: J Power and Energy* 2001; 215: 507–512.

6. Guha A. Optimum fan pressure ratio for bypass engines with separate or mixed exhaust streams. *AIAA J Propul Power* 2001; 17: 1117–1122.

7. Rice W. Tesla turbomachinery. In: E Logan (ed.) *Handbook of turbomachinery*. New York: Marcel Dekker, pp.861–874.

8. Guha A and Sengupta S. The fluid dynamics of the rotating flow in a Tesla disc turbine. *Eur J Mech B/ Fluids* 2013; 37: 112–123.

9. Guha A. Structure of partly dispersed normal shock waves in vapour-droplet flows. *Phys Fluids A* 1992; 4: 1566–1578.

10. Guha A. Jump conditions across normal shock waves in pure vapour droplet flows. *J Fluid Mech* 1992; 241: 349–369.

11. Guha A. A unified theory of aerodynamic and condensation shock waves in vapour-droplet flows with or without a carrier gas. *Phys Fluids A* 1994; 6: 1893–1913.

12. Guha A. A unified theory for the interpretation of total pressure and temperature in two-phase flows at subsonic and supersonic speeds. *Proc R Soc* 1998; 454: 671–695.

13. Guha A. Computation, analysis and theory of two-phase flows. *Aeronaut J* 1998; 102: 71–82.

14. Song J, Gu CW and Li XS. Performance estimation of Tesla turbine applied in small scale Organic Rankine Cycle (ORC) system. *Appl Therm Eng* 2017; 110: 318–326.

15. Carey VP. Assessment of Tesla turbine performance for small scale Rankine combined heat and power systems. *J Eng Gas Turbines Power* 2010; 132: 122301–1:8.

16. Hoya GP and Guha A. The design of a test rig and study of the performance and efficiency of a Tesla disc turbine. *Proc. IMechE, Part A: J Power and Energy* 2009; 223: 451–465.

17. Lemma E, Deam RT, Toncich D, et al. Characterisation of a small viscous flow turbine. *J Exp Therm Fluid Sci* 2008; 33: 96–105.

18. McGarey S and Monson P. *Performance and efficiency of disk turbines*. MEng Research Project Report (Advisor: A Guha), Report No. 1203, University of Bristol, UK, 2007.

19. Guha A and Sengupta S. The fluid dynamics of work transfer in the non-uniform viscous rotating flow within a Tesla disc turbomachine. *Phys Fluids* 2014; 26: 033601–1:27.

20. Guha A and Sengupta S. The physics of pressure variation in microchannels within corotating or static discs. *Phys Fluids* 2016; 28: 103601–1:19.

21. Boyd KE and Rice W. Laminar inward flow of an incompressible fluid between rotating disks, with full peripheral admission. *J Appl Mech* 1968; 35: 229–237.

22. Herrmann-Priesnitz B, Calderón-Muñoz WR, Salas EA, et al. Hydrodynamic structure of the boundary layers in a rotating cylindrical cavity with radial inflow. *Phys Fluids* 2016; 28: 033601–1:16.

23. Sengupta S and Guha A. A theory of Tesla disc turbines. *Proc. IMechE, Part A: J Power and Energy* 2012; 226: 650–663.

24. Guha A and Sengupta S. Similitude and scaling laws for the rotating flow between concentric discs. *Proc IMechE, Part A: J Power and Energy* 2014; 228: 429–439.

25. Zhao D, Ji C, Teo C, et al. Performance of small-scale bladeless electromagnetic energy harvesters driven by water or air. *Energy* 2014; 74: 99–108.

26. Lampart P and Jedrzejewski Ł. Investigations of aerodynamics of Tesla bladeless microturbines. *J Theoret Appl Mech* 2011; 49: 477–499.

27. Abrahamson SD, Eaton JK and Koga DJ. The flow between shrouded corotating disks. *Phys Fluids A* 1989; 1: 241–251.

28. Schuler CA, Usry W, Weber B, et al. On the flow in the unobstructed space between shrouded corotating disks. *Phys Fluids A* 1990; 2: 1760–1770.

29. Huang RF and Hsieh MK. Phase-resolved flow characteristics between two shrouded co-rotating disks. *Exp Fluids* 2011; 51: 1529–1547.

30. Wu SC. A PIV study of co-rotating disks flow in a fixed cylindrical enclosure. *Exp Therm Fluid Sci* 2009; 33: 875–882.

31. Soong CY, Wu CC, Liu TP, et al. Flow structure between two co-axial disks rotating independently. *Exp Therm Fluid Sci* 2003; 27: 295–311.

32. Hendriks F. On Taylor vortices and Ekman layers in flow-induced vibration of hard disk drives. *Microsyst Technol* 2010; 16: 93–101.

33. Shirai K, Yaguchi Y, Büttner L, et al. Highly spatially resolving laser Doppler velocity measurements of the tip clearance flow inside a hard disk drive model. *Exp Fluids* 2011; 50: 573–586.

34. Czarny O, Iacovides H and Launder BE. Precessing vortex structures in turbulent flow within rotor-stator disc cavities. *Flow Turbul Combust* 2002; 69: 51–61.

35. Nore C, Tartar M, Daube O, et al. Survey of instability thresholds of flow between exactly counter-rotating disks. *J Fluid Mech* 2004; 511: 45–65.

36. Hewitt RE and Al-Azhari M. Non-axisymmetric self-similar flow between two rotating disks. *J Eng Math* 2009; 63: 259–277.

37. Sengupta S and Guha A. Analytical and computational solutions for three-dimensional flow-field and relative pathlines for the rotating flow in a Tesla disc turbine. *Comput Fluids* 2013; 88: 344–353.

38. ANSYS. *Theory guide of ANSYS CFX 15*. Canonsburg, PA: ANSYS, Inc., 2013.

39. Rhie CM and Chow WL. A numerical study of the turbulent flow past an isolated airfoil with trailing edge separation. In: *3rd Joint thermophysics, fluids, plasma and heat transfer conference*, St. Louis, MO, USA. AIAA-82-0998, 1982.